cy^{2}

AXIAL-FORCE MEASUREMENTS ON CONE CYLINDERS MOUNTED IN A SIMULATED AEROBALLISTIC RANGE TRACK IN TUNNEL F WITH APPLICATION TO A FULL-SCALE SYSTEM

VON KÁRMÁN GAS DYNAMICS FACILITY
ARNOLD ENGINEERING DEVELOPMENT CENTER
AIR FORCE SYSTEMS COMMAND
ARNOLD AIR FORCE STATION, TENNESSEE 37389

August 1975

Final Report for Period June 1, 1974 to January 20, 1975

Prepared for

DIRECTORATE OF TECHNOLOGY
ARNOLD ENGINEERING DEVELOPMENT CENTER
ARNOLD AIR FORCE STATION, TENNESSEE 37389

This report has been reviewed by the Information Office (OI) and is releasable to the National Technical Information Service (NTIS). At NTIS, it will be available to the general public, including foreign nations.

APPROVAL STATEMENT

This technical report has been reviewed and is approved for publication.

FOR THE COMMANDER
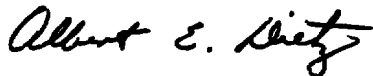
ALBERT E. DIETZ
Requirements Planning
    Division
Directorate of Technology

ROBERT O. DIETZ
Director of Technology

UNCLASSIFIED

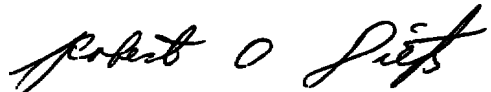| REPORT DOCUMENTATION PAGE		READ INSTRUCTIONS BEFORE COMPLETING FORM
1 REPORT NUMBER AEDC-TR-75-78	**2 GOVT ACCESSION NO.**	**3 RECIPIENT'S CATALOG NUMBER**
4 TITLE (and Subtitle) AXIAL—FORCE MEASUREMENTS ON CONE CYLINDERS MOUNTED IN A SIMULATED AEROBALLISTIC RANGE TRACK IN TUNNEL F WITH APPLICATION TO A FULL—SCALE SYSTEM		**5 TYPE OF REPORT & PERIOD COVERED** Final Report – June 1, 1974 to January 20, 1975
		6. PERFORMING ORG REPORT NUMBER
7 AUTHOR(s) David E. Boylan, ARO, Inc.		**8. CONTRACT OR GRANT NUMBER(s)**
9 PERFORMING ORGANIZATION NAME AND ADDRESS Arnold Engineering Development Center (DY) Air Force Systems Command Arnold Air Force Station, Tennessee 37389		**10 PROGRAM ELEMENT, PROJECT, TASK AREA & WORK UNIT NUMBERS** Program Element 65807F
11 CONTROLLING OFFICE NAME AND ADDRESS Arnold Engineering Development Center (DYFS), Arnold Air Force Station, Tennessee 37389		**12. REPORT DATE** August 1975
		13. NUMBER OF PAGES 63
14 MONITORING AGENCY NAME & ADDRESS(if different from Controlling Office)		**15. SECURITY CLASS. (of this report)** UNCLASSIFIED
		15a. DECLASSIFICATION/DOWNGRADING SCHEDULE N/A

16 DISTRIBUTION STATEMENT (of this Report)

Approved for public release; distribution unlimited.

17 DISTRIBUTION STATEMENT (of the abstract entered in Block 20, if different from Report)

18 SUPPLEMENTARY NOTES

Available in DDC.

19. KEY WORDS (Continue on reverse side if necessary and identify by block number)

conical bodies	shock wave interaction
aerodynamic forces	hypervelocity testing techniques
aeroballistics	simulation testing
ranges (facilities)	wind tunnel tests
drag	

20 ABSTRACT (Continue on reverse side if necessary and identify by block number)

Axial—force measurements on cone—cylinder models mounted in a simulated aeroballistic range model restraining track system are presented. The data were obtained in the range $15.4 \lesssim M_\infty < 19.2$ at Reynolds numbers between 0.29 and 1.08 x 10^6 per foot. An analytical technique based on inviscid conical flow-field solutions and the experimental data was used to develop an empirical method for estimating the contribution to the model drag from the interaction of the model bow shock on the track system and its subsequent

DD FORM 1 JAN 73 **1473** EDITION OF 1 NOV 65 IS OBSOLETE

UNCLASSIFIED

20. ABSTRACT (Continued)

reflections back onto the model surface. It is shown that about 15 to 40 percent of total vehicle drag (neglecting sliding friction between the model and the track rails) will be from this shock interaction contribution. Important parameters are cone angle, nose bluntness, model velocity, track dimensions, and range pressure. Calculations are performed over the expected envelope of operation for a full-scale test facility.

AFSC
Arnold AFS Tenn

PREFACE

The work herein was conducted by the Arnold Engineering Development Center (AEDC), Air Force Systems Command (AFSC). The work was done by ARO, Inc. (a subsidiary of Sverdrup & Parcel and Associates, Inc.), contract operator of AEDC, AFSC, Arnold Air Force Station, Tennessee. The work was conducted under ARO Project No. V31S-36A. The author of this report was David E. Boylan, ARO, Inc. The manuscript (ARO Control No. ARO-VKF-TR-75-31) was submitted for publication on March 14, 1975.

The author wishes to acknowledge the efforts of Mr. H. R. Little, of the von Kármán Gas Dynamics Facility (VKF) Test Operation Branch, in design and fabrication of the test models, Mrs. Betty Majors, of the VKF Projects Branch, for programming of the analysis, and Mr. Glen Norfleet, Manager of the VKF Aeroballistics Branch, for his helpful suggestions during the course of the analysis.

CONTENTS

ILLUSTRATIONS

TABLES

1.0 INTRODUCTION

Deceleration measurements on a 45-deg sharp cone cylinder traveling in a constraining track mechanism at McDonnell Douglas Astronautics Company (MDAC) at Huntington Beach, California (Ref. 1), revealed increases in "apparent" vehicle drag. The two obvious sources of added drag appear to be sliding friction drag caused by a portion of the cylinder bearing on one or more of the constraining tracks and drag caused by bow shock reflections off the track impinging back onto the model cone surface. The design of future experiments and tracks for the Hyperballistic Ranges (G and K) of the von Kármán Gas Dynamics Facility (VKF) or a full-scale reentry facility depends, in part, on the isolation of the cause of this added drag and the evaluation of the relative magnitudes of the aerodynamic bow shock and sliding friction sources.

A simulated track mechanism was constructed and tested in Tunnel F using a sharp 45-deg and a slightly blunted 10-deg cone-cylinder as model configurations. One-component axial-force measurements were made with and without the track mechanism in place. Design of the track simulated range environment as closely as possible and ensured that any increase in measured drag could be only from sources induced by the model bow shock system and/or the shock system originating from the rail leading edge.

2.0 TEST ARTICLE AND WIND TUNNEL

2.1 TEST ARTICLE

Two cone-cylinder models were tested with and without a constraining track designed from existing model and track dimensions of the McDonnell Douglas experiment. Model and track dimensions are given in Fig. 1. A photograph of the 10-deg model mounted on the one-component force balance with the track mechanism in place is shown in Fig. 2. Within constraints, the track rails could be positioned at varying distances relative to the force models. An electric circuit ensured that no contact between model and track was made during a test run. In addition to these models, a 1-in.-diam hemisphere-cylinder with an overall length of 2.75 in. was tested. This model was instrumented with a stagnation point pressure gage which allowed local tunnel flow properties to be obtained. Axial-force and p_o' measurements were obtained with this model.

It was recognized that complete simulation of the range environment was not possible because of the leading-edge shock generated from the track mechanism interacting with the model and model shock. The leading edge of the track mechanism was designed with a knife edge (Figs. 1 and 2) for this reason. The influence of track leading-edge position
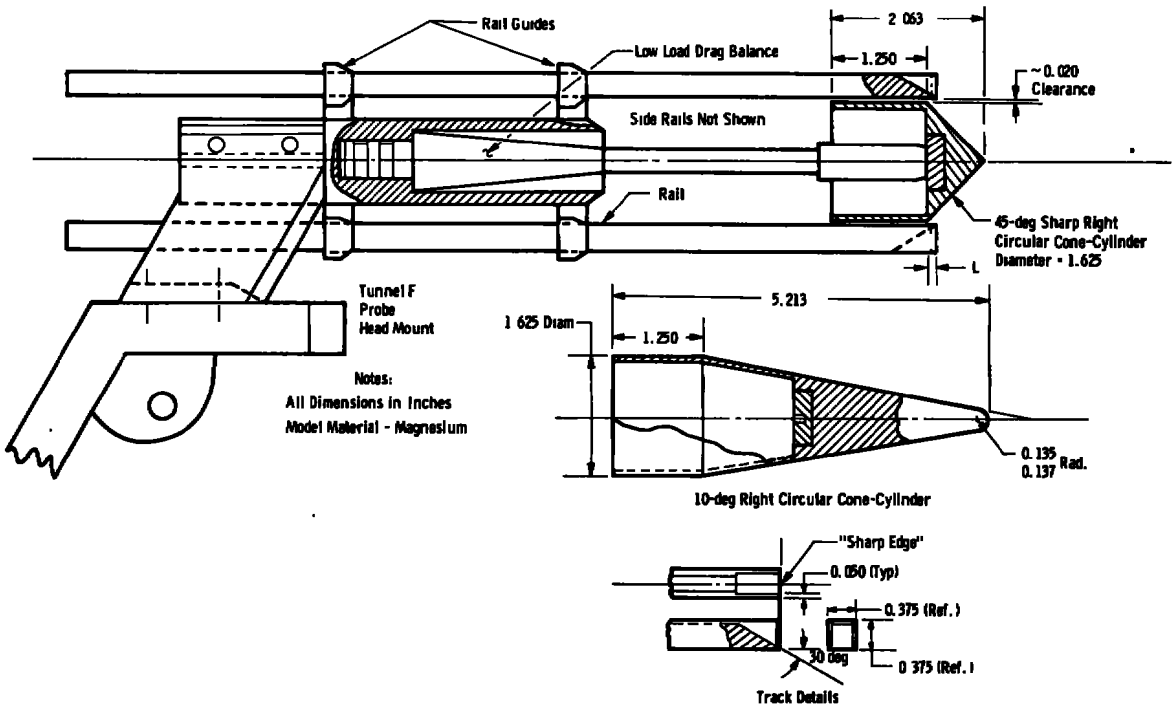
Figure 1. Sketch of models and track.
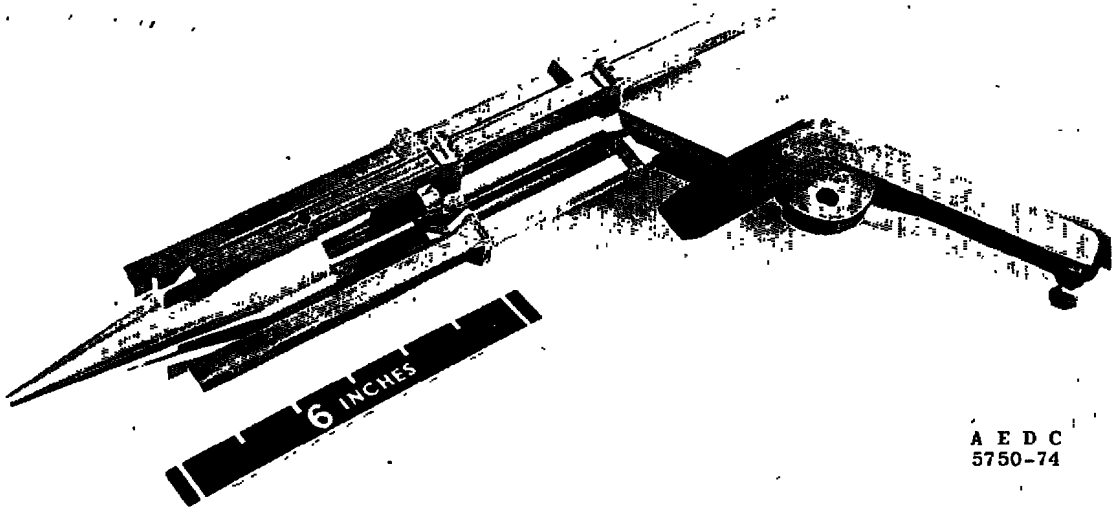
Figure 2. 10-deg model mounted in track mechanism.

relative to the model affected the amounts of shock spreading* and boundary-layer growth on the track ahead of the model. These factors were expected to influence the Tunnel F data but would not exist on the range track. Later analysis of the data considers these factors, and the data are corrected for their influence.

2.2 ·TUNNEL AND NOZZLE DESCRIPTION

The Hypervelocity Wind Tunnel (F) is an arc-driven wind tunnel of the hotshot type (Ref. 2) and is capable of providing Mach numbers from about 7.5 to 20 over a Reynolds number-per-foot range from 0.05 x 10^6 to 70 x 10^6. Test sections of 108-in. diameter (M_∞ = 14 to 20) and 54-in. diameter (M_∞ = 10 to 17) are available using a 4-deg, half-angle conical nozzle. The range of Mach numbers at a particular test station in the conical nozzle is obtained by using various throat diameters. The M_∞ = 8 and 12 contoured nozzles have 25-in. and 40-in. exit diameters, respectively, which connect to the 54-in.-diam test station and provide a free-jet exhaust. The test gas for aerodynamic and aerothermodynamic testing is nitrogen. Air is used for combustion tests. The test gas is confined in either a 1.0-ft^3, a 2.5-ft^3, or a 4.0-ft^3 arc chamber, where it is heated and compressed by an electric arc discharge. The increase in pressure results in a diaphragm rupture, with the subsequent flow expansion through the nozzle. Test times are typically from 50 to 200 msec. Shadowgraph and schlieren coverage are available at both test sections.

This test was conducted in the 108-in.-diam test section of the conical nozzle for M_∞ = 15.4 to 19.2. Nitrogen was the test gas. The 1.0- and 2.5-ft^3 arc chambers were used, and useful test times up to approximately 120 msec were obtained. Because of the relatively short test times, the model wall temperature remained essentially invariant from the initial value of approximately 300°K; thus $T_w/T_o \approx 0.1$ and approximates the condition of practical interest for reentry vehicles.

3.0 INSTRUMENTATION AND TEST PROCEDURES

3.1 INSTRUMENTATION

Axial-force measurements were obtained using a one-component, low load internal balance which is 1.5 in. long and 0.50 in. in diameter. A calibration was performed before the test entry to determine whether interactions were present. None could be detected under the largest conceivable normal or side forces. Static loads from 0.007 to 2.123

---

*The term "shock spreading" refers to the increasing area on the model cone surface which is influenced by the rail lip shocks as the rail is extended forward of the model shoulder.

lbf were applied to determine the balance calibration constant. Absolute measurement uncertainty was determined from calibration repeatability and is estimated as ±0.001 lbf.

Test section flow conditions were monitored with 1.0-in.-diam hemisphere-cylinders instrumented with slug calorimeters and pitot probes. In addition to the monitor probes, the hemisphere-cylinder model mentioned above was instrumentated with a sealed, miniature semiconducter strain gage-type pressure transducer.

Detailed information concerning the force, heat-transfer, and pressure instrumentation can be found in Refs. 3 and 4.

3.2 PROCEDURES

The large size of the Tunnel F test section allowed the test to be conducted concurrently with a sponsored force test using spare instrumentation channels. The model was placed either 13 in. below or 12-7/8 in. above the tunnel centerline, depending on requirements dictated by the primary test article located on the nozzle centerline (Fig. 3). The model was adjusted to the local velocity vector, and the model nose was near the window vertical centerline for all runs. Test variables included flow condition, model, and track location. Table 1 summarizes the range and combination of variables studied.
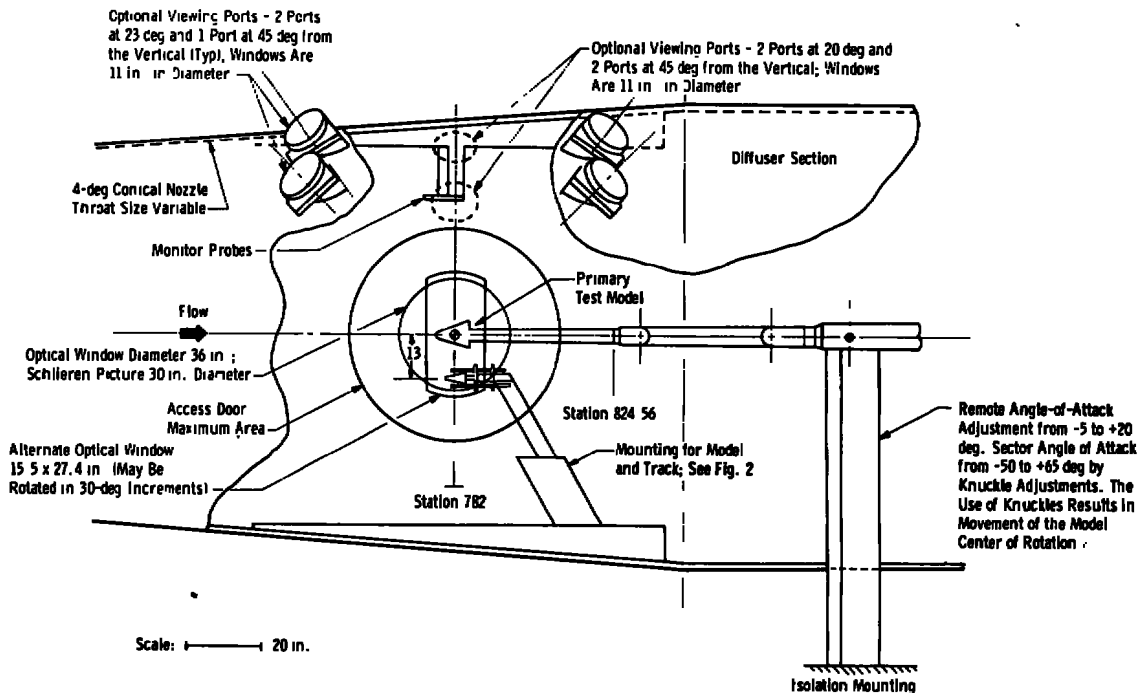
Figure 3. Schematic of Tunnel F 108-in. test section.

10

Table 1. Test Matrix

Run	Model	L, in.	M_∞ (Approximate)	Re/ft x 10^{-6}
4788	Hemisphere Cylinder	Track Not Used	18.5	0.47 − 0.85
4789	Calibration Body	↓	19.5	0.42 − 1.08
4790	Calibration Body	↓	19.0	0.39 − 0.65
4791	10-deg Blunt Cone	Not in Place	18.5	0.49 − 0.80
4792	Cylinder	Not in Place	19.2	0.42 − 0.50
4793		0.50	19.0	0.51 − 0.89
4795		0.75	19.5	0.39 − 0.68
4812		0.75	16.2	0.60 − 1.58
4816		0.75	15.5	0.73 − 1.24
4800		1.50	19.0	0.44 − 0.73
4794		3.96	19.0	0.41 − 0.57
4799		3.96	19.2	0.43 − 0.68
4796	↓	3.96*	18.8	0.39 − 0.70
4802	45-deg Sharp Cone	Not in Place	15.4	0.22 − 0.49
4806	Cylinder	↓	15.6	0.30 − 0.49
4817		↓	15.6	0.34 − 0.72
4805		1.15	16.0	0.37 − 0.52
4804		0.35	15.6	0.34 − 0.67
4803		0.81	15.8	0.32 − 0.79
4808		2.00	15.3	0.25 − 0.74
4819		2.00	15.7	0.32 − 0.58
4807	↓	3.68	15.5	0.29 − 0.66

*Three Rails Removed

3.2.1 Test Conditions

The method of determining the tunnel flow conditions is briefly summarized as follows: instantaneous values of reservoir pressure, p_o, and free-stream pitot pressure, p_o', are measured, and an instantaneous value of the stagnation heat-transfer rate, $\dot{q}_o$, is inferred from a direct measurement of a shoulder heat rate on a 1.0-in.-diam hemisphere-cylinder heat probe. Total enthalpy, Ho, is calculated from p_o', $\dot{q}_o$, and the heat probe radius,

using Fay-Riddell theory (Ref. 5). The value of Ho determined in this manner and the measured value of reservoir pressure is then used to determine corresponding values of reservoir temperature, density, and entropy from tabulated thermodynamic data for nitrogen (Ref. 6). The reservoir conditions, the measured value of p'_o, and the assumption of isentropic flow in the nozzle are then used to compute the free-stream conditions. The basic procedure followed in this computation is given in Refs. 7 and 8.

3.2.2 Data Acquisition

Acquisition of test data was accomplished using a digital system with concomitant oscillographs for analog records. The digital data system is capable of scanning 70 data channels in one millisecond and can store up to 150 scans of data. Basic data reduction is done on an off-line digital computer.

4.0 DATA PRECISION

The uncertainties in the calculated force data were estimated by using the Taylor series method of error propagation to combine the uncertainties in each measurement occurring in the calculation. In general, it is estimated that for nominal loads the uncertainty in the force measurement is ±6 percent. This uncertainty includes calibration linearity and repeatability, instrumentation system error, and errors introduced by dynamic effects resulting from the impulsive operating nature of the facility. For nominal load situations, the uncertainty of ±6 percent of the balance component measurement combined with a ±4-percent uncertainty in the dynamic pressure gives an uncertainty in C_{A_t} of ±7 percent.

Laboratory calibrations using static loads indicate that the pressure transducers are accurate to ±1 percent. Similarly, the uncertainties in the heat-transfer-rate gages are ±5 percent. The uncertainties in measured data, however, are higher because of the dynamics of the measurements and systems errors. The uncertainties in the monitor probe measurements, p'_o and $\dot{q}_o$, and arc-chamber measurement, p_o, were estimated considering both the static calibrations and the repeatability of the test section calibration profile. The uncertainties in the pressure data (p'_o and p_o) are estimated to be ±4 percent and ±5 percent, respectively, based on an average of two measurements each, and the heat-transfer rate, $\dot{q}_o$, is ±5 percent based on an average of four measurements. These values were used to estimate uncertainties in the tunnel flow parameters using the Taylor method of error propagation. Representative parameters are given below.

Uncertainty (±), percent

M_∞	Re/ft	T_∞	p_∞	q_∞
1.5	10	6	6	4

The model attitude position was set prior to each run, and the pitch angles are estimated to be accurate within ±0.20 deg.

The effect of placing a model in conical source flow was examined since the measurements presented in this report were obtained in a conical nozzle at an off-centerline position. A source flow calculation indicated that a maximum error of 0.6 percent in C_{A_t} would result for the 10-deg cone-cylinder model, with smaller errors for the 45-deg cone-cylinder model. Considering the small size of this correction and the uncertainty of the force coefficients themselves, these corrections were not applied to the data presented herein. All axial-force data represent total measured axial force. No adjustments for base pressure effects have been made, and no base pressure measurements were obtained.

5.0 RESULTS AND DISCUSSION

Although it was recognized that model bow shock location in relation to the constraining track would be of primary importance, it was not possible to utilize the tunnel optics as an accurate measurement device. The demands of coverage on the primary test model located on the tunnel centerline and the need for schlieren movies of this model resulted in poor coverage, with few good quality schlieren stills of the secondary models and track system. No high quality coverage was obtained on the 45-deg sharp cone-cylinder model. Figure 4 indicates two of the better shock pattern photographs with the 10-deg cone-cylinder model at two track positions. It can be observed that the model bow shock was not completely captured for the rail position of 0.75 in. from the shoulder, whereas the 1.50-in. position exhibited complete capture well downstream of the rail leading edge. Although the rails appear to have a blunt leading edge in Fig. 4, this is not the case (see Figs. 1 and 2). A knife edge was fabricated to lessen rail leading-edge shock effects since a true range environment would not produce such a shock system. It will be demonstrated in Section 6.0 that the schlieren coverage shown in Fig. 4 was very important in analysis of the data and its application to a full-scale track system.

Axial-force measurements on the hemisphere-cylinder calibration body were in excellent agreement with previously published data (Ref. 9). These data are not presented herein since they would serve no useful purpose in the present analysis.

In order to define a "baseline" value for later determination of the effect of the track rail system, several runs were made with the 10-deg blunt cone-cylinder and the 45-deg sharp cone-cylinder with the track mechanism completely removed. Typical data from these runs are tabulated in Table 2 and shown in Fig. 5. The dimension "ℓ" used in calculation of the parameter $M_\infty / \sqrt{Re_\ell}$ is defined for each model in this figure.

Run 4816, L = 0.75 in.

Run 4800, L = 1.50 in.
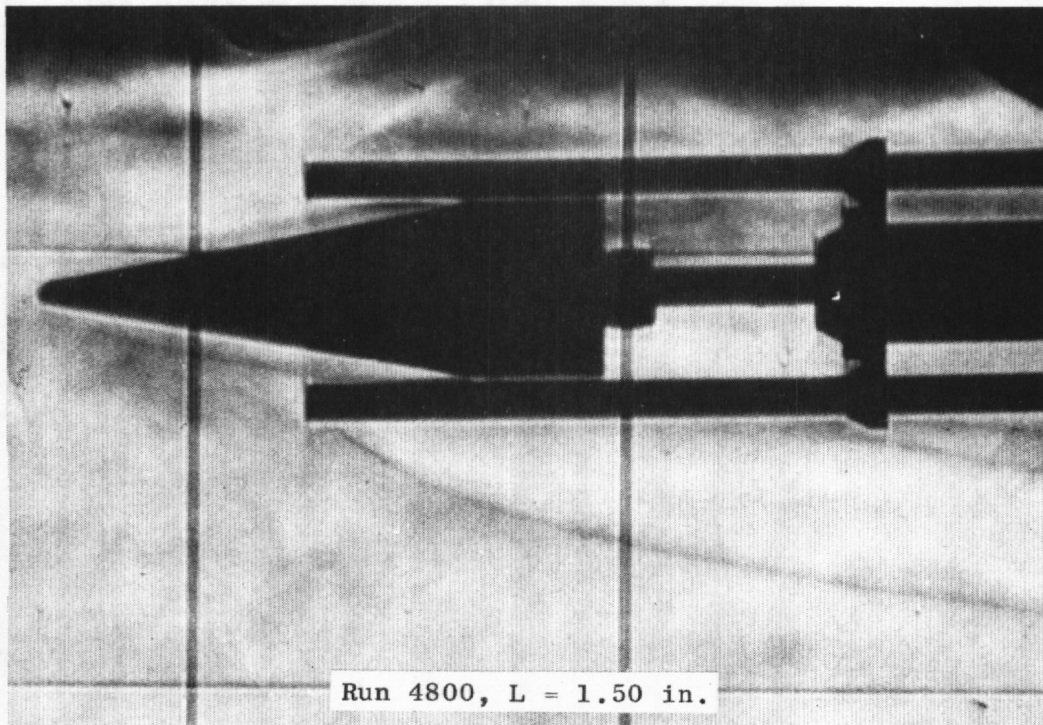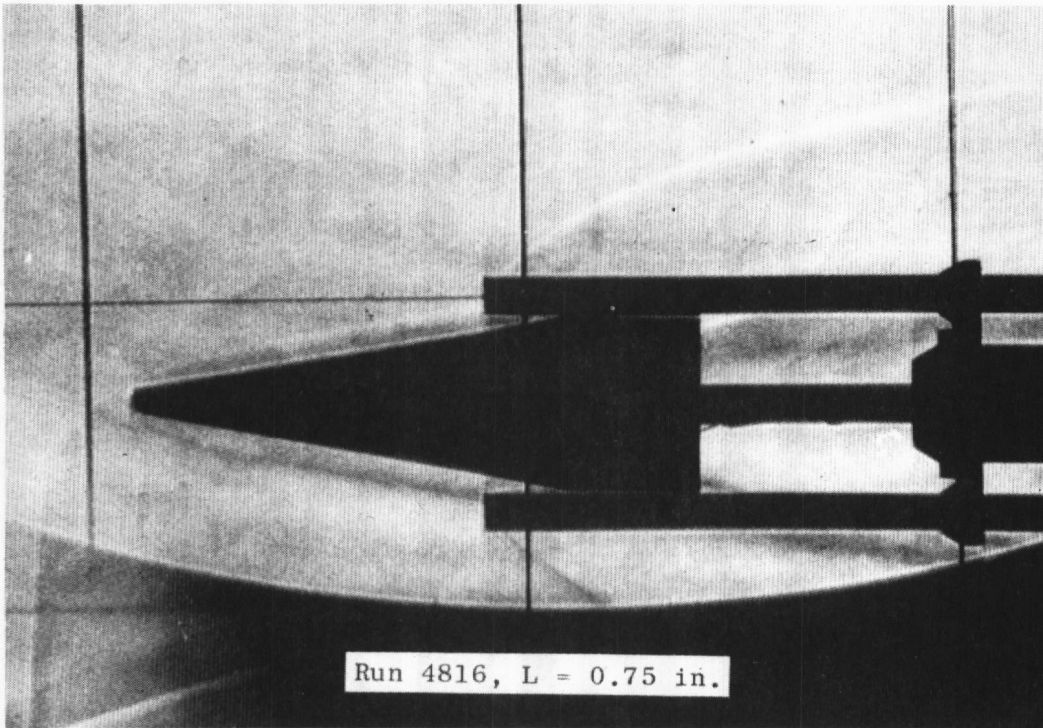
Figure 4. Schlieren coverage of the 10-deg cone-cylinder model
with two rail positions.

Table 2. Flow Conditions and Axial-Force Data with No Track System in Place

Model	Run	Time, msec	P_o, psia	T_o, °R	p_∞, psia	T_∞, °R	V_∞, ft/sec	q_∞, psia	M_∞	Re/ft x 10^{-6}	C_{A_t}
10-deg Blunt Cone-Cylinder	4791	50	22.764	4,667	0.00525	75.4	8,324	1.357	19.2	0.799	0.126
		60	20,758	5,121	0.00500	85.9	8,716	1.246	18.9	0.615	0.135
		80	17,061	4,885	0.00452	83.1	8,467	1.099	18.7	0.576	0.152
		90	15,624	4,837	0.00436	83.3	8,407	1.043	18.5	0.551	0.159
		100	14,109	4,725	0.00420	82.4	8,289	0.987	18.3	0.534	0.163
		110	13,010	4,759	0.00396	83.6	8,307	0.921	18.2	0.490	0.166
	4792	90	15,443	4,775	0.00333	76.1	8,353	0.860	19.2	0.500	0.152
	4792	110	12,728	4,730	0.00272	75.0	8,284	0.700	19.2	0.417	0.152
45-deg Sharp Cone-Cylinder	4802	60	5,363	3,852	0.00494	88.0	7,316	0.848	15.6	0.486	1.066
		70	4,909	4,378	0.00463	103.9	7,837	0.771	15.4	0.350	1.055
		80	4,565	4,810	0.00427	116.7	8,245	0.700	15.3	0.269	1.083
		90	4,177	4,858	0.00382	117.4	8,286	0.628	15.3	0.239	1.092
		100	3,860	4,689	0.00338	110.9	8,127	0.566	15.5	0.232	1.083
		110	3,553	4,570	0.00305	106.7	8,011	0.515	15.6	0.223	1.075
	4806	80	4,529	3,548	0.00433	80.3	6,986	0.741	15.6	0.488	0.961
		100	3,880	3,897	0.00365	89.8	7,344	0.618	15.6	0.346	0.988
		110	3,572	3,901	0.00339	90.1	7,344	0.572	15.5	0.319	0.961
		120	3,329	3,901	0.00300	88.8	7,343	0.513	15.6	0.291	0.973
	4817	70	5,439	3,209	0.00529	71.2	6,622	0.916	15.7	0.718	0.928
		80	5,084	3,638	0.00478	82.4	7,087	0.820	15.7	0.519	0.934
		90	4,669	3,857	0.00431	88.2	7,313	0.737	15.6	0.414	0.935
		100	4,340	4,034	0.00391	92.5	7,490	0.667	15.6	0.356	0.933
		110	4,011	3,944	0.00357	89.7	7,395	0.613	15.7	0.342	0.935

Since the present measurements were made in relatively low free-stream Reynolds number conditions, second-order viscous shear stress effects on the aerodynamic drag influenced the results. The author could find no previous data on blunt cone-cylinders in this particular flow regime although there are numerous sets of data available on blunt cones. Since the cylinder portion of the 10-deg blunt cone model represented about 25 percent of its axial length, it could be expected that this portion of the model would increase the viscous drag significantly. Previous data on blunt cones suggest that total drag should be from 1.4 to 1.7 times the inviscid pressure drag. A calculation of this latter parameter (C_{A_i}) using the method of Ref. 10 and a Newtonian proportionality constant of 1.833 gave a value of 0.081. Thus, based on previous cone data and approximate analytic results, a measured axial-force coefficient of 0.11 to 0.14 could be expected on the 10-deg blunt cone cylinder with no track interference. The influence of viscous drag on the cylindrical portion of the model would increase this value somewhat.

For the case of the 45-deg sharp cone-cylinder model, previous data from the VKF Low Density Hypersonic Wind Tunnel (L) and Tunnel C and a Langley hypersonic tunnel using 40-, 45-, and 50-deg sharp cones suggest that very little if any viscous contribution to the total drag would be present at the free-stream Reynolds numbers of the present test. An inviscid solution from Ref. 11 indicates that an axial-force coefficient, C_{A_i}, of 1.06 would be measured on a 45-deg sharp cone with no cylindrical afterbody. The viscous drag on the cylindrical afterbody could be expected to increase this value slightly.

Data from Runs 4802, 4806, and 4817 (Table 2)

$$\ell = \ell_1 + \ell_2 = 2.400 \text{ in.}$$

45-deg Sharp Cone-Cylinder

Data Fairing

C_{A_t}

C_{A_i}

$M_\infty / \sqrt{Re_\ell}$

Data from Runs 4791 and 4792 (Table 2)

Data Fairing

$$\ell = 5.213 \text{ in.}$$

10-deg Blunt Cone-Cylinder

C_{A_t}

C_{A_i}

$M_\infty / \sqrt{Re_\ell}$
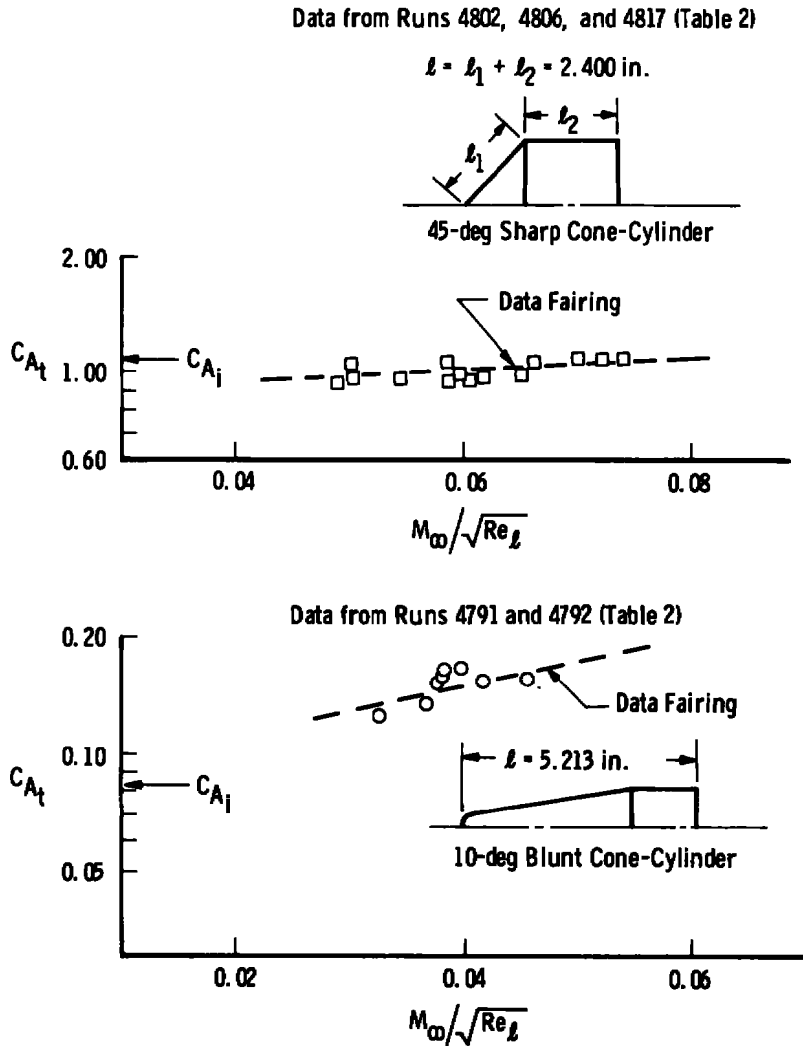
Figure 5. Axial-force measurements with no track system in place.

The data for both the 10-deg slightly blunted cone-cylinder and the 45-deg sharp cone-cylinder are in good agreement with these analytic and experimental estimates. The fairings of the experimental results shown in Fig. 5 serve as the baseline values for later analysis of the effect of the simulated track mechanism on shock-induced (shock interference) drag.

Results of axial-force measurements with the 45-deg sharp cone-cylinder model with the track system in place at varying locations relative to the model shoulder are tabulated in Table 3 and shown in Fig. 6. Although viscous drag influence was small, the data are shown as a function of $M_\infty / \sqrt{Re_\ell}$ for convenience.

16

**Table 3. Flow Conditions and Axial-Force Data on
45-deg Sharp Cone-Cylinder with Track**

Run	Time, msec	P_o, psia	T_{∞}, °R	P_{∞}, psia	T_{∞}, °R	V_{∞}, ft/sec	q_{∞}, psia	M_{∞}	Re/ft x 10^{-6}	L, in.	C_{A_t}
4805	80	4,812	3,476	0.00419	76.1	6,911	0.739	15.9	0.519	0.15	1.027
	90	4,426	3,352	0.00379	72.5	6,772	0.675	16.0	0.508		1.019
	100	4,122	3,249	0.00354	69.8	6,653	0.632	16.0	0.503		1.019
	110	3,826	3,326	0.00345	72.9	6,735	0.605	15.8	0.455		1.024
	120	3,559	3,645	0.00349	83.6	7,077	0.588	15.5	0.367		1.028
4804	60	5,571	3,362	0.00581	77.0	6,793	0.981	15.5	0.670	0.35	1.167
	70	5,155	3,807	0.00523	89.1	7,264	0.872	15.4	9.498		1.161
	80	4,788	4,126	0.00464	97.2	7,587	0.774	15.4	0.388		1.185
	90	4,413	4,100	0.00408	95.2	7,559	0.689	15.5	0.354		1.192
	100	4,071	3,967	0.00363	90.4	7,420	0.622	15.7	0.343		1.171
4803	70	4,687	2,812	0.00453	60.6	6,152	0.797	15.9	0.791	0.81	1.244
	80	4,406	3,254	0.00411	71.7	6,662	0.717	15.8	0.585		1.252
	90	4,103	3,483	0.00367	77.0	6,911	0.642	15.8	0.446		1.254
	100	3,823	3,649	0.00329	80.7	7,087	0.577	15.8	0.373		1.254
	110	3,542	3,773	0.00302	83.8	7,213	0.528	15.8	0.323		1.257
4808	70	4,817	3,137	0.00532	71.9	6,531	0.889	15.5	0.735	2.00	1.139
	80	4,542	3,753	0.00479	88.5	7,200	0.790	15.4	0.459		1.116
	90	4,172	4,073	0.00434	97.6	7,525	0.709	15.3	0.357		1.148
	100	3,853	4,309	0.00400	104.7	7,757	0.647	15.2	0.294		1.167
	110	3,572	4,495	0.00378	111.0	7,933	0.604	15.1	0.254		1.176
4819	70	5,442	3,541	0.00506	79.4	6,988	0.876	15.7	0.584	2.00	1.148
	80	5,066	4,059	0.00449	92.8	7,525	0.770	15.7	0.415		1.158
	90	4,647	4,135	0.00398	94.1	7,597	0.688	15.7	0.356		1.157
	100	4,279	4,018	0.00358	90.2	7,474	0.625	15.8	0.343		1.147
	110	3,964	4,043	0.00334	90.5	7,475	0.581	15.8	0.318		1.137
4807	60	5,117	3,334	0.00569	77.6	6,755	0.942	15.4	0.664	3.68	1.229
	70	4,761	3,796	0.00494	89.4	7,249	0.818	15.4	0.467		1.227
	80	4,454	4,018	0.00429	93.8	7,473	0.719	15.5	0.388		1.253
	90	4,093	4,149	0.00381	96.8	7,604	0.641	15.5	0.322		1.294
	100	3,813	4,126	0.00343	95.1	7,577	0.583	15.6	0.298		1.297
	110	3,519	4,027	0.00318	92.5	7,474	0.542	15.6	0.290		1.259

A shadowgraph supplied by McDonnell Douglas on the 45-deg models indicated that the interaction of the bow shock with the track would be a Mach reflection and that a triple intersection would occur. A sketch of the shadowgraph is shown in Fig. 7. Scaling this figure produced a distance of 0.35 in. from the shoulder for the intersection of the Mach reflection and track. An examination of the schlieren results from run 4805 (L = 0.15) indicated that no interaction of the model bow shock and the "inside" of the rail occurred. The small increased drag for small value of L is therefore not surprising. The quality of the schlieren from run 4804 (L = 0.35) did not allow a good determination of shock interaction location. However, Fig. 7 (from lower Mach number flow) indicated that the interaction should have been completed at this track position. A 17-percent increase in aerodynamic drag was measured from this run. Track data from McDonnell Douglas on a 45-deg sharp cone-cylinder indicated approximately a 26-percent increase,

but friction forces between the track rails and the cylinder portion of the model may have been present in the track experiments, and flow conditions (M_∞ and Re/ft) were considerably different.
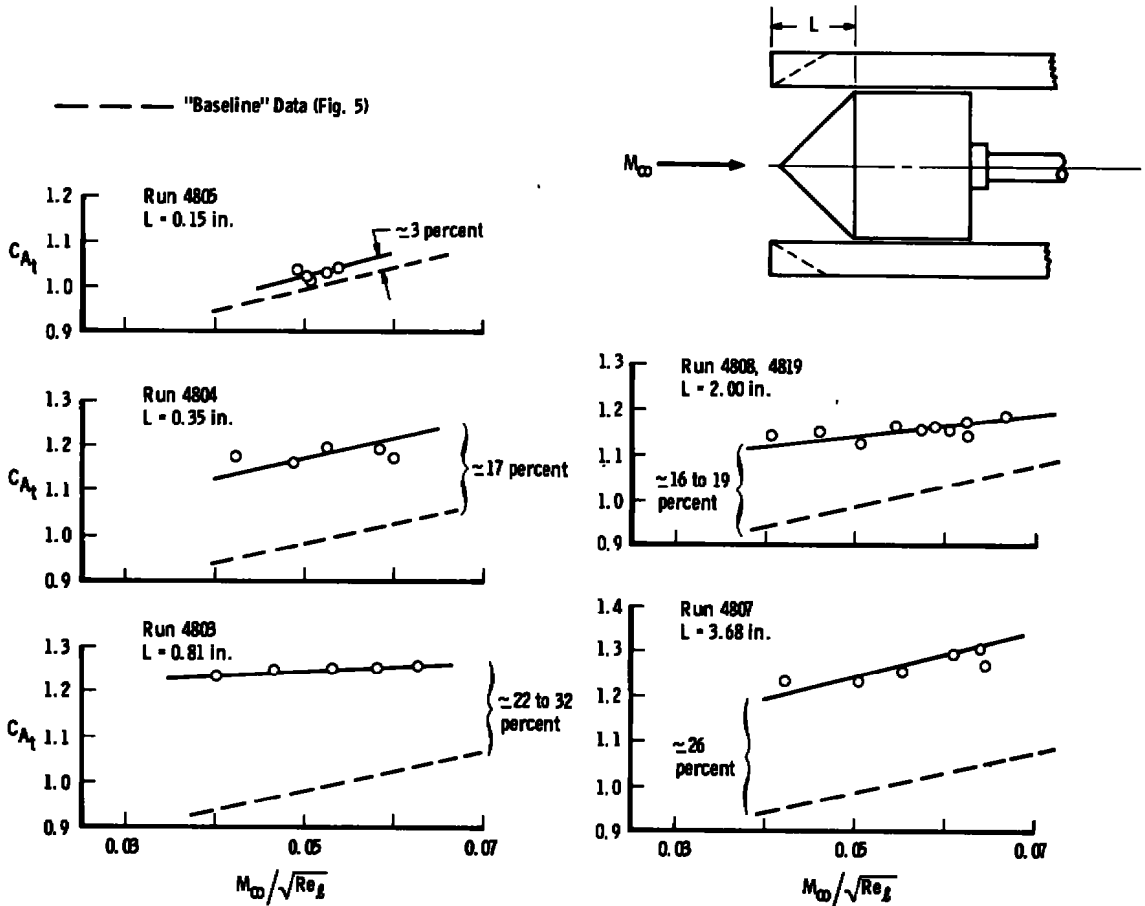
Figure 6. Axial-force measurements on the 45-deg sharp cone-cylinder with track system in place.

The observed increase in total axial drag in Fig. 6 as the track leading edge was further extended suggests a strong influence of the shock system induced by the rail leading edge and boundary-layer growth on the rail surface. Neither of these would be present in an actual aeroballistic range environment, and they would prevent direct application of the present data to a range track without modification.

Results of axial-force measurements with the 10-deg blunt cone-cylinder model with the track system in place at varying locations relative to the model shoulder are tabulated in Table 4 and shown in Fig. 8. Since this model was influenced by viscous shear forces, the data are plotted as a function of $M_\infty/\sqrt{Re_\ell}$.
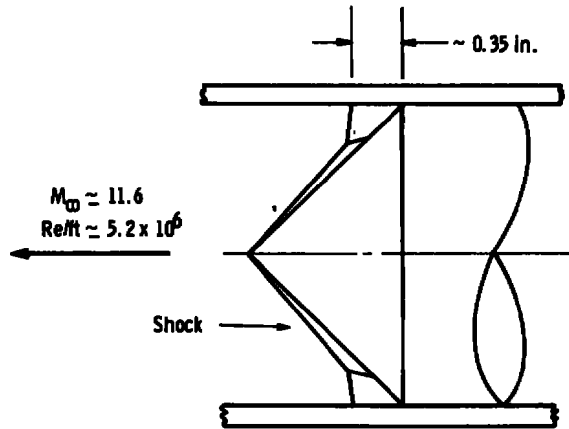
Figure 7. Sketch of shadowgraph from McDonnell Douglas track test.

Table 4. Flow Conditions and Axial-Force Data on
10-deg Blunt Cone-Cylinder with Track

Run	Time, msec	p_o, psia	T_o, °R	p_∞, psia	T_∞, °R	V_∞, ft/sec	q_∞, psia	M_∞	Re/ft x 10⁻⁶	L, in.	C_{A_t}
4793	60	19,924	3,985	0.00390	59.0	7,640	1.087	20.0	0.891	0.50	0.140
	70	18,542	4,172	0.00385	63.6	7,811	1.041	19.7	0.775		0.144
	80	16,723	4,358	0.00395	69.6	7,970	1.014	19.2	0.676		0.146
	100	13,897	4,603	0.00404	79.1	8,172	0.960	18.4	0.549		0.143
	110	12,529	4,586	0.00381	79.8	8,142	0.892	18.3	0.507		0.147
4795	80	16,585	4,077	0.00296	59.1	7,697	0.836	20.1	0.679	0.75	0.176
	90	15,339	4,352	0.00294	65.5	7,955	0.799	19.7	0.567		0.183
	100	14,105	4,646	0.00293	72.7	8,220	0.766	19.3	0.473		0.187
	110	12,845	4,716	0.00286	75.6	8,272	0.729	19.1	0.431		0.191
	120	11,872	4,826	0.00278	78.9	8,363	0.692	18.9	0.388		0.192
4812	60	13,076	3,245	0.01056	68.5	6,759	1.984	16.4	1.584	0.75	0.123
	70	12,032	3,901	0.00915	84.6	7,445	1.687	16.2	0.990		0.135
	80	10,834	3,982	0.00801	86.1	7,515	1.479	16.2	0.845		0.143
	90	9,891	4,165	0.00733	91.1	7,688	1.338	16.1	0.706		0.149
	100	8,916	4,352	0.00704	98.1	7,860	1.249	15.9	0.599		0.153
4816	50	13,064	3,605	0.01286	82.6	7,145	2.239	15.8	1.242	0.75	0.119
	60	11,959	4,579	0.01168	111.1	8,105	1.944	15.4	0.798		0.139
	70	10,845	4,646	0.01113	114.8	8,155	1.815	15.3	0.717		0.153
	80	9,768	4,381	0.01026	107.3	7,891	1.677	15.3	0.732		0.162
4800	50	21,627	4,608	0.00435	71.4	8,261	1.170	19.6	0.734	1.50	0.188
	70	17,704	4,572	0.00405	73.3	8,186	1.042	19.2	0.642		0.203
	80	16,000	4,615	0.00395	75.7	8,207	0.988	18.9	0.587		0.209
	90	14,485	4,664	0.00375	77.8	8,236	0.920	18.9	0.531		0.211
	100	12,888	4,702	0.00352	79.8	8,235	0.846	18.5	0.475		0.218
	110	11,729	4,685	0.00324	79.7	8,228	0.774	18.5	0.436		0.225
4794	70	18,259	4,867	0.00389	77.7	8,446	1.009	19.3	0.567	3.96	0.254
	80	16,467	4,799	0.00358	76.8	8,386	0.922	19.2	0.530		0.237
	90	14,930	4,405	0.00330	69.2	7,997	0.859	19.3	0.573		0.234
	100	13,658	4,408	0.00310	69.9	7,989	0.798	19.2	0.529		0.241
	110	12,376	4,792	0.00282	77.6	8,336	0.710	19.0	0.406		0.273
4799	60	19,733	4,534	0.00378	69.0	8,173	1.032	19.7	0.676	3.96	0.224
	70	18,223	4,761	0.00358	73.8	8,370	0.955	19.5	0.571		0.237
	80	16,456	4,874	0.00349	77.7	8,455	0.903	19.2	0.508		0.249
	100	13,739	4,838	0.00333	80.0	8,392	0.826	18.8	0.455		0.257
	110	12,534	4,756	0.00310	78.7	8,303	0.764	18.8	0.432		0.256
4796	50	21,821	4,972	0.00545	83.6	8,592	1.356	18.9	0.698	3.96*	0.167
	70	17,509	5,123	0.00415	85.5	8,688	1.032	18.8	0.513		0.177
	90	14,177	4,901	0.00354	82.0	8,454	0.869	18.7	0.463		0.182
	100	12,877	4,871	0.00321	81.3	8,414	0.786	18.7	0.425		0.187
	110	11,580	4,788	0.00279	78.8	8,325	0.690	18.8	0.389		0.196

*Three Rails Removed
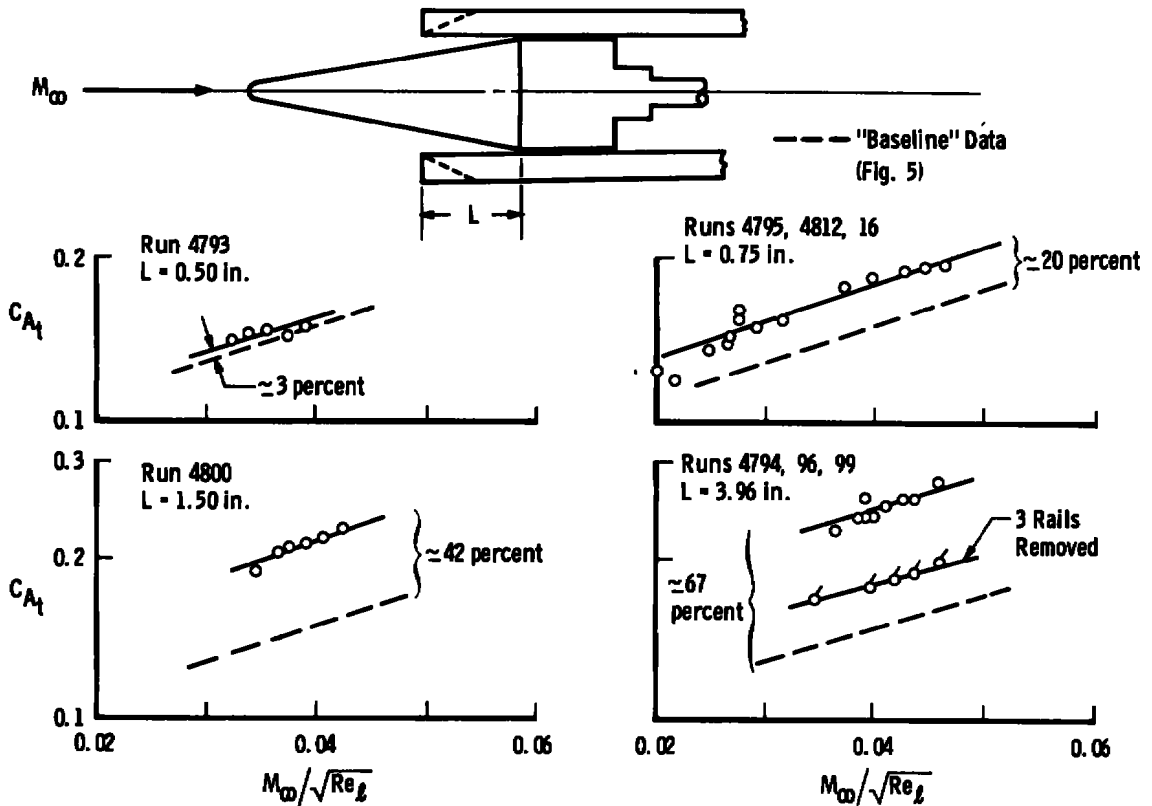
**Figure 8. Axial-force measurements on the 10-deg blunt cone-cylinder with track system in place.**

The increase in aerodynamic drag due to the reflection of the model bow shock from the rail back onto the model is seen to be quite significant. From an examination of the schlieren results, it was concluded that the bow shock was not completely captured for L = 0.750 in. and that it interacted just downstream of the track leading edge at ·L = 1.50 in. (Fig.4). The fact that the drag continued to rise as the leading edge of the track extended forward suggested again that the track leading-edge shock and/or the boundary-layer growth on the track at the location of the model did violate simulation of the range environment. In this regard, these data are discussed in more detail in Section 6.0. There are as yet no range data to compare to these measurements.

6.0 APPLICATION OF TUNNEL F DATA IN DETERMINATION OF SHOCK INTERFERENCE DRAG ON A FULL-SCALE TRACK SYSTEM

The total drag coefficient, C_{D_T}, experienced by a spherically blunted cone-cylinder launched at zero angle of attack in a range and constrained by a track system is the sum of the component drag coefficients expressed as

$$\underbrace{C_{D_T} = C_{D_P} + C_{D_V} + C_{D_B} + C_{D_{IP}}}_{\text{aerodynamic forces}} + \underbrace{C_{D_{SI}} + C_{D_F}}_{\text{track related forces}} = \frac{\text{Total Drag}}{q_\infty A} \quad (1)$$

The first four components are standard aerodynamic forces--namely pressure drag, viscous drag, base drag, and viscous induced pressure drag. The term $C_{D_{SI}}$ is the contribution caused by the influence of the upstream shock system on the track rail and the subsequent interaction on the model surface. The term C_{D_F} is the contribution of the sliding friction force between the cylinder and the rails of the track. The present experimental program attempted to measure the term $C_{D_{SI}}$ for two particular cone geometries. The term C_{D_F} was intentionally kept at zero.

It was proposed that the Tunnel F experimental data be scaled to other track dimensions and other model geometries and a parametric study be conducted to determine the magnitude of the shock interaction drag at typical range conditions. It was also requested that the study be limited to sharp or slightly blunted slender cones.

Each of the terms in Eq. (1) will be discussed. However, the method by which the term $C_{D_{SI}}$ is determined will be discussed in some detail. Future studies, with additional experimental data, will no doubt improve the present analysis. Terms related to track-induced drag forces are discussed first.

6.1 SHOCK INTERFERENCE DRAG

The evaluation of the term $C_{D_{SI}}$ in Eq. (1) and its relative importance to the other terms of the equation is the primary purpose of the present study. The basic mechanism of the induced drag on the model due to the reflection of the model bow shock from the rail back on to the surface of the model and subsequent reflections between the model and the track rail can be seen in Fig. 9. This analysis and discussion is limited to sharp or slightly blunted slender cones at Mach numbers sufficiently high that the local flow in the vicinity of the track rail is supersonic and the reflection is of a "like sense" (Ref. 13) so that the angle of reflection equals the angle of incidence. This stipulation removes the experimental data obtained using the 45-deg sharp cone from the present discussion. The ranges of variables suggested for study were $5 \lesssim \theta_c \lesssim 30$ deg and $0 \lesssim \xi \lesssim 0.3$. Therefore, the analysis does depend greatly on the data obtained using the slightly blunted ($\xi = 0.167$) 10-deg cone model. For a model of finite bluntness, the shock approaching the track rail is neither straight nor two-dimensional. A rigorous analysis should account for shock curvature and local flow gradients. An example is shown in Fig. 10 which compares perfect gas method of characteristics solutions** ($M_\infty = 14$ and 20) to inviscid

---

**Solutions obtained by E. R. Marchand, Special Studies Group, VKF.

flow-field sharp-cone solutions (Ref. 11). This figure is drawn to scale for the present 10-deg blunt cone with the track leading edge placed 1.50 in. from the cone shoulder. A previously discussed schlieren photograph (Fig. 4) obtained during run 4800 indicates good agreement between observed and calculated shock shape.
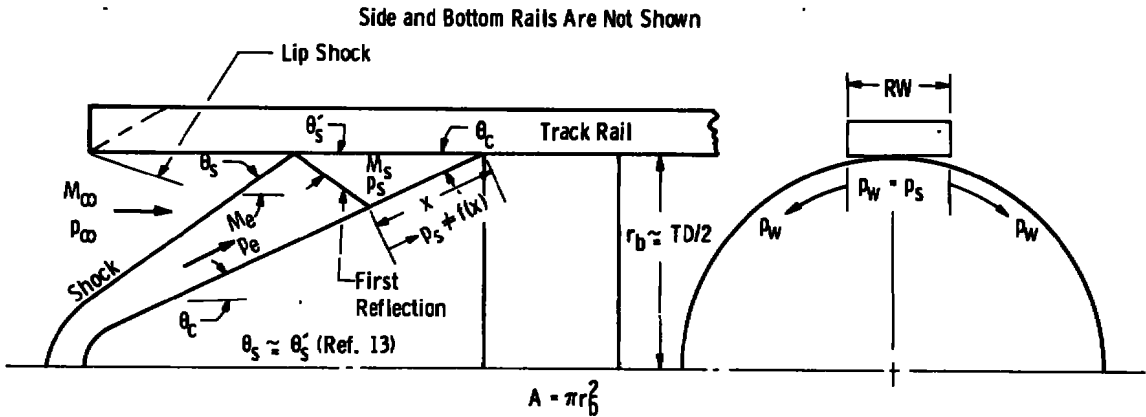
Figure 9. Simplified shock mechanism.
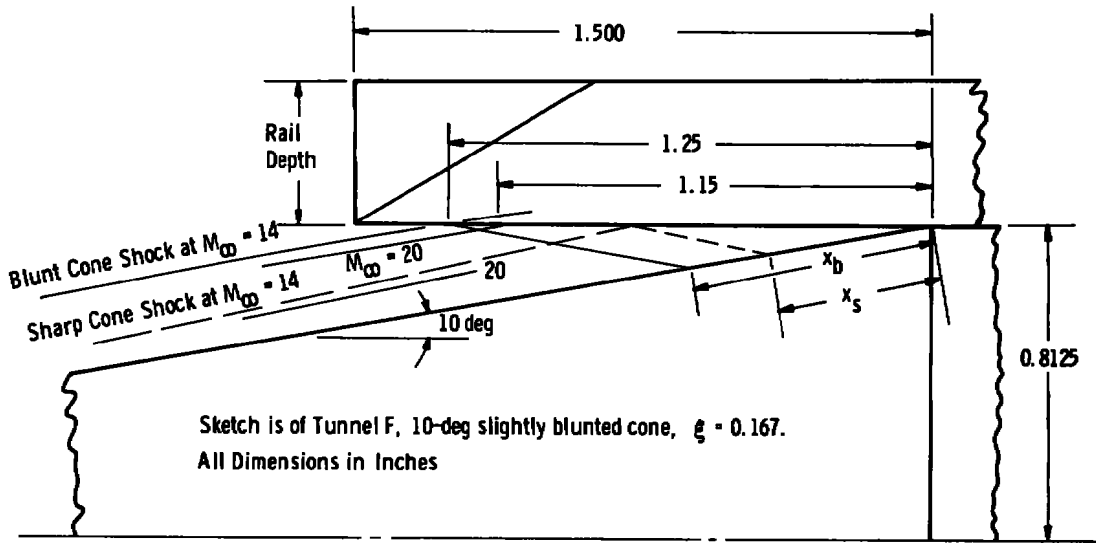
Note: Lip shock from track rail is not shown.

**Figure 10. Comparison of blunt and sharp cone shock shapes
in reflection region.**

Although it was recognized that a blunt bow shock analysis would be of more practical value, it was not attempted because a large number of characteristic solutions would be required. Also, shock shape is sensitive to real gas effects, but all calculations in the present analysis assume perfect gas relationships. An example of perfect and real gas shock shapes

is shown in Fig. 11. It was felt that the lack of experimental data would prevent an evaluation of the rigorous approach even if the increased effort was undertaken to obtain the numerous necessary solutions. The present analysis assumes that the local pressure, p_s (Fig. 9), and the geometric length, x, can be computed by crossing two inviscid flow-field conical shock systems. It should be noted that the reflected shock would more nearly be plane since it is from a two-dimensional surface. However, using this model greatly simplifies the numerical work required for the analysis.
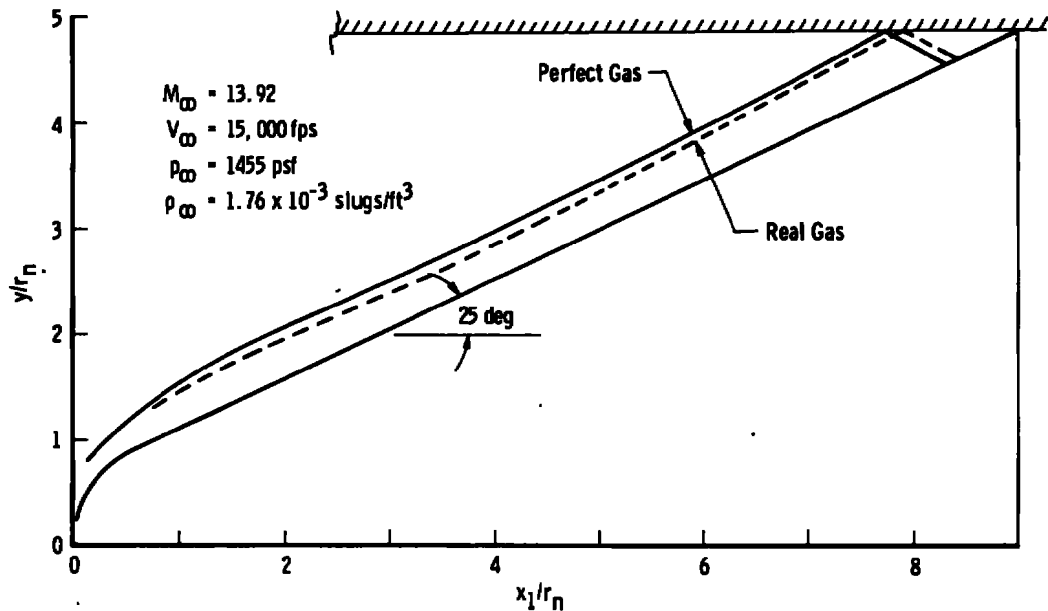
Figure 11. Perfect and real gas shock shapes.

As Fig. 9 indicates, the drag (neglecting the lip shock) induced by the bow shock reflection system can be written

$$D_{SI} = 4K \ (x) \ (p_s/p_\infty) \ (p_\infty) \ (RW) \tag{2}$$

and

$$C_{D_{SI}} = D_{SI}/q_\infty A \tag{3}$$

where

1. $(p_s/p_\infty)(p_\infty)$ is the average pressure in the reflection region and is assumed to be the value after the first reflection (subsequent reflections ignored);

2. x is the cone surface distance from the first reflection to the shoulder (Fig. 9), RW is the width of the rail, and the constant 4 is included because a four rail track system was used (The term 4(x)(RW) is therefore the affected shock area influenced by the pressure p_s);

3. K is a complex correction factor which must be empirically derived from available data to account for the simplification of the model, lip shock contribution, and second-order effects. (The parameter should also allow a range of model configurations and track dimension to be studied.)

This model implicitly assumes a step change in local surface pressure, p_s, down to a normal cone surface pressure, p_w, at the edge of each rail (Fig. 9). It also ignores the influence caused by the model bow shock interacting with the sides of the rail and thereby causing a local increase in model pressure. The empirical constant K could be expected to be a strong function of the product $(x)(p_s/p_\infty)$, cone angle and bluntness, and Mach number, and a weaker function of rail width and rail depth. Experimental data presented earlier served as the basis for evaluating the constant K in Eq. (2). Since this is basic to the present analysis, a discussion of its evaluation is given in some detail.

To be completely valid, this constant should be used only for the geometry and flow conditions for which the data were obtained; i.e.,

$$15.2 \lesssim M_\infty \lesssim 20.1$$

$$\theta_c = 10 \text{ deg}$$

$$\xi = 0.167$$

laminar boundary-layer conditions

The present task demanded that a method be devised which would allow calculation of D_{SI} for other geometric and flow conditions; i.e.,

$$5 \lesssim \theta_c \lesssim 30$$

$$6.5 \lesssim M_\infty \lesssim 20$$

$$0 \lesssim \xi \lesssim 0.3$$

turbulent boundary-layer conditions and
range temperatures and pressure conditions

The method which is used in accomplishing this is also discussed below. The need for additional experimental data will be apparent in this regard.

6.1.1 Determination of the Constant K

The drag measurements discussed in Section 5 and shown in Fig. 8 are used in the determination of the parameter K. Intuitive reasoning suggests that the track location which "more nearly" simulates a range environment would be at the position for which the model bow shock just intersects the bottom of the track rail. In other words, complete capture of the shock system is desired with no excess track length to allow bounday-layer growth or lip shock effects to excessively influence the data. Three runs were made with the track leading edge 0.750 in. in front of the cone shoulder, and a consistent 20-percent increase in drag was measured. However, a post-test analysis of both characteristic blunt body shock shape solutions and schlierien photographs strongly suggests that incomplete capture of the shock system resulted at this rail location (Figs. 4 and 10).

· A cross plot of the 10-deg cone drag measurements as a function of rail position is shown in Fig. 12. From characteristics solutions (Fig. 10) it was inferred that placing
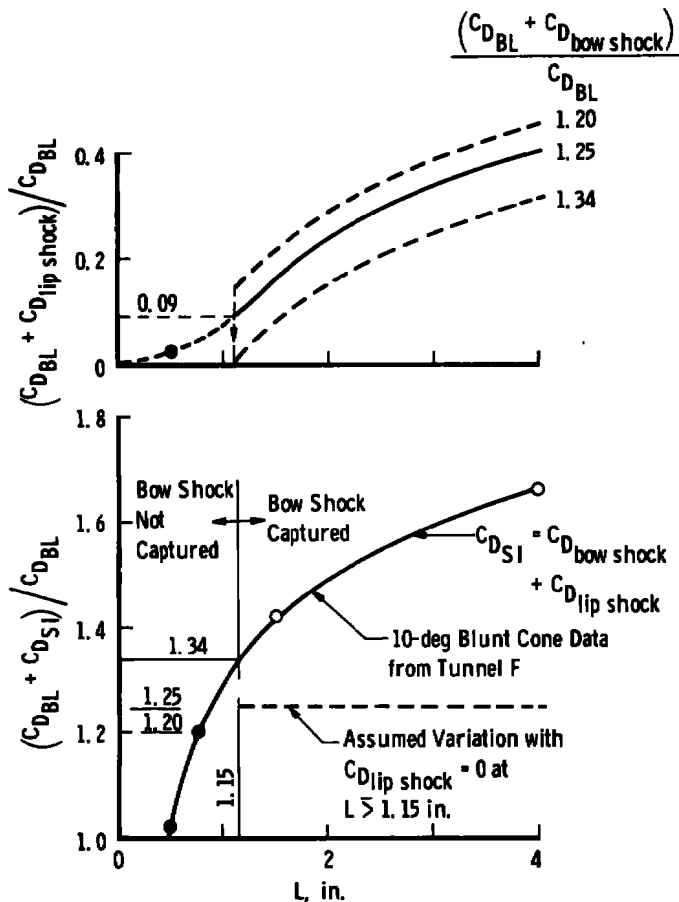
Figure 12. Interpretation of 10-deg cone data used in solution of the parameter K.

the rail at about 1.15 in. upstream of the cone-cylinder function would have been the optimum location. The manner in which the data are presented in Fig. 12 implicitly assumes that the observed increase in drag which resulted when the rails were in position was entirely due to the increased pressure on the cone induced by the model bow and rail lip shock and that none of the other terms in Eq. (1) was affected by the presence of the track. Therefore, the differential between the baseline data and the total drag would represent the contribution of of the track system and be, by definition. $C_{D_{SI}}$. From Fig. 12, at L = 1.15, this results in

$$C_{D_{SI}} = 1.34 \ C_{D_{BL}} - C_{D_{BL}} = 0.34 \ C_{D_{BL}} \tag{4}$$

where $C_{D_{BL}}$ can be read, for a given value of $M_{\infty}/\sqrt{Re\ell}$, from Fig. 5. However, the contribution of the rail lip shock is also included in the total shock interaction drag component. and it would therefore be conservative to apply this result to an actual track system. To correct for this tunnel-induced effect, it was assumed that once the bow shock was completely captured, no further increase in drag due to bow shock interaction would result.[†] However. lip shock drag would continue to increase with L since boundary-layer and shock spreading would increase. By making the additional assumption that the increase over the drag measured at L = 0.50 was due largely to rail lip shock drag, one could estimate the individual contributions of model bow shock and lip shock. The technique is shown graphically in Fig. 12. In the range from 1.20 to 1.34, various values of

$$(C_{D_{BL}} + C_{D_{BOW \ SHOCK}})/C_{D_{BL}}$$

were tried until a reasonable variation of lip shock drag with rail position L was found. The resulting value gave a correction of 0.09 from the total measured value of 1.34, which is about a 7-percent correction at L = 1.15 in. Although the technique and assumptions used are not by any means rigorous, the resulting correction is not large, and a better method could probably not be devised with the given experimental data. A final value of $C_{D_{SI}}$, where only the bow shock is considered, is therefore

$$C_{D_{SI}} = 0.25 \ C_{D_{BL}} \tag{5}$$

and

$$D_{SI} = (0.25 \ C_{D_{BL}}) (q_{\infty}A) \tag{6}$$

[†] This interpretation of the data was suggested by Mr. Glen Norfleet, Manager of the VKF Aeroballistic Branch.

For a given Tunnel F run, where $C_{D_{BL}}$ is known, the parameter K can be obtained from Eqs. (2), (3), and (6) and is expressed as

$$K = \frac{0.25 \, C_{D_{BL}} \, q_\infty A}{4(p_s/p_\infty)(p_\infty)(x)(RW)} \tag{7}$$

Equation (7) was evaluated at discrete time points for runs 4795, 4800, and 4816, which represented the extreme range of q_∞, M_∞, and p_∞ used during the present test. The term p_s/p_∞ and x were hand calculated from the conical inviscid flow-field solutions of Jones (Ref. 11). The results were as follows:

Run	Number of Time Points	Average M_∞	Average K
4795	5	19.42	0.52 ± 0.03
4800	6	18.90	0.49 ± 0.04
4816	4	15.45	0.35 ± 0.03

This variation of K was initially very disturbing since the observed strong Mach number influence was not expected. A value for K of unity would have resulted if all flow model assumptions were correct and second-order effects such as interaction of the shock off the rail side wall, boundary-layer change, base pressure effect, etc. were small. Considering the relative simplicity of the flow model, the absolute values from 0.35 to 0.52 were not surprising.

The variation of K with Mach number was explained when it was realized that K was very sensitive to changes in the product $(x)(p_s/p_\infty)$. A two-step conical shock solution was performed for a 10-deg sharp cone in the range $3 \lesssim M_\infty \lesssim 30$,[‡] and the resulting variation of $(x)(p_s/p_\infty)$ is shown in Fig. 13, as is the variation of K. Dimensional analysis suggested use of the parameter $M_\infty \sin \theta_c$ as the dependent variable. Since the calculation was performed for a specific cone geometry, the parameter $(x)(p_s/p_\infty)$ has the units of length. However, only the slope and not the absolute value is of interest, and the results could therefore be used for other cone base diameters. The parameter K, in part, corrects the flow model for the error induced by using sharp conical shock relationships rather than blunt body characteristics solutions in calculating the shock area $4(x)(RW)$ and local pressure, p_s. One would expect this error to increase as Mach number decreases, as is indicated by the results in Fig. 13. A few experimental points at low Mach numbers ($M_\infty \approx 8$) would verify this. The experimentally derived values of K plotted as a function of $M_\infty \sin \theta_c$ were then faired using the slope of the $(x)(p_s/p_\infty)$ curve. A curve fit of the variation of K shown in Fig. 13 yields the empirical cubic relationship

---

[‡]The wide Mach number variation was necessary for reasons explained later.

$$K \approx 0.07795 - 0.02892 \, M_\infty \sin \theta_c + 0.05204 \, M_\infty^2 \sin^2 \theta_c - 0.000841 \, M_\infty^3 \sin^3 \theta_c \quad (8)$$

It should be noted that this relationship is valid only in the range $3 \leqslant M_\infty \leqslant 30$ and for a 10-deg blunt cone with $\xi = 0.167$.
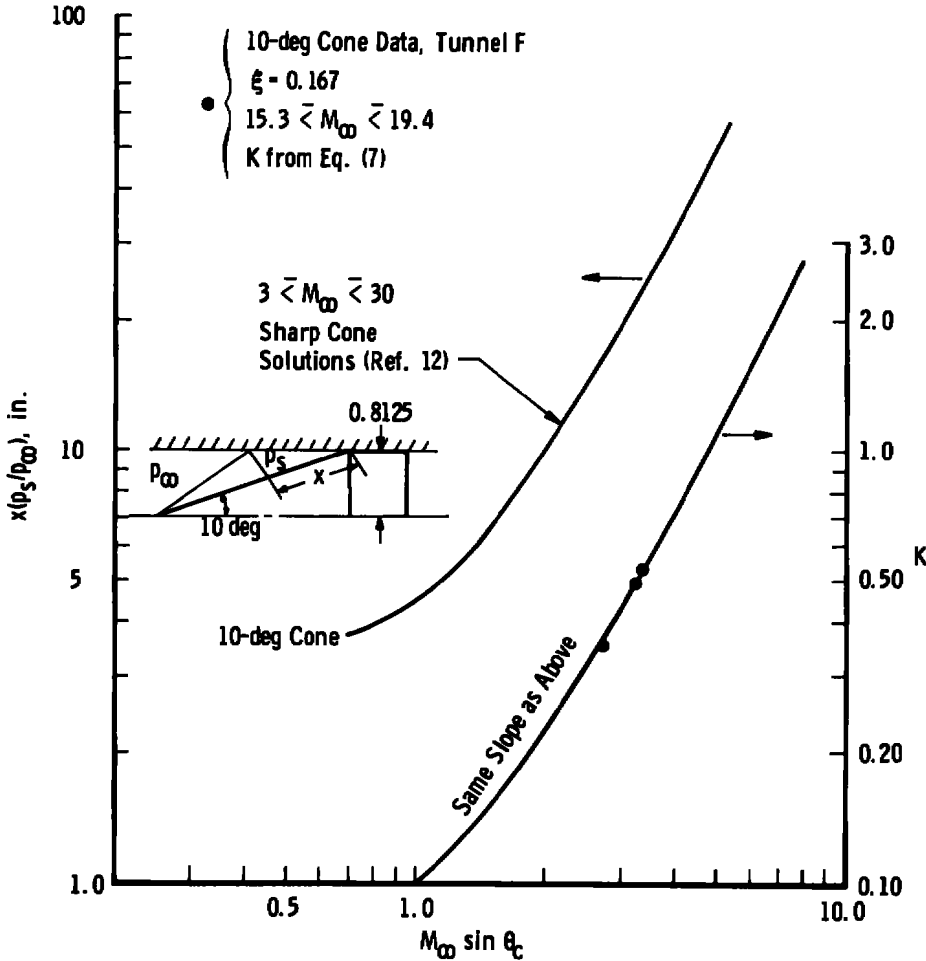
Figure 13. Empirical constant K as determined from Tunnel F data and conical inviscid flow-field solutions.

6.1.2 Derivation of K for Cone Angles Other Than 10 deg with $\xi = 0.167$

Since it is obvious that the term $(x)(p_s/p_\infty)$ is sensitive to Mach number for a given cone angle, it was assumed that for a given Mach number it would be sensitive to cone angle. An evaluation of shock interference drag on models with cone angles between 5 and 30 deg was desired. To permit this, two-step inviscid flow-field sharp cone solutions using the tables of Ref. 11 were again performed (for $6 \lesssim M_\infty \lesssim 20$), and the results are shown in Fig. 14. It can be observed that the ratio of $(x)(p_s/p_\infty)$ for a cone angle

θ_c to that for a 10-deg cone is independent of $M_\infty \sin \theta_c$ (Fig. 15). If it is then again assumed that the empirical constant K is a strong function of $(x)(p_s/p_\infty)$ and Mach number and only a weak function of track width, Eq. (8) can be corrected for cone angles other than 10 deg by the empirical parameter Y defined in Fig. 15 and given by the relationship

$$Y \approx 8.1775/(\theta_c)^{0.9105} \qquad (9)$$

where θ_c is in degrees.
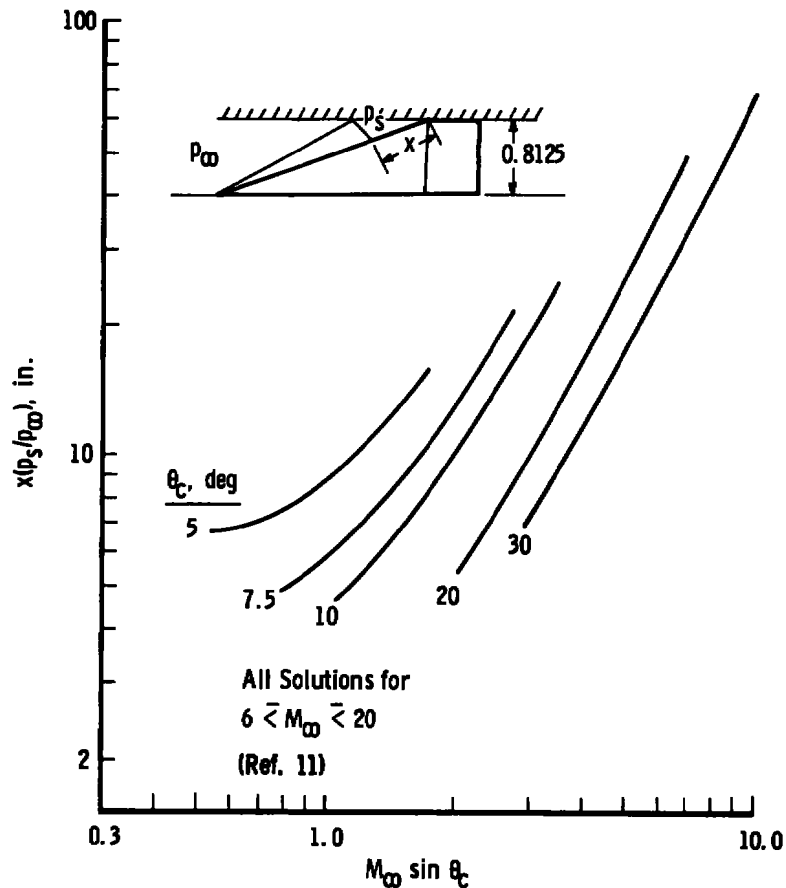
Figure 14. Family of cone solutions.

Since Y = 1.0 for θ_c = 10 deg, the empirical constant K for an arbitrary cone angle θ_c with bluntness ratio 0.167 (in the range $6 \lesssim M_\infty \lesssim 20$, $5 \lesssim \theta_c \lesssim 30$ deg) is the product of Eqs. (8) and (9).
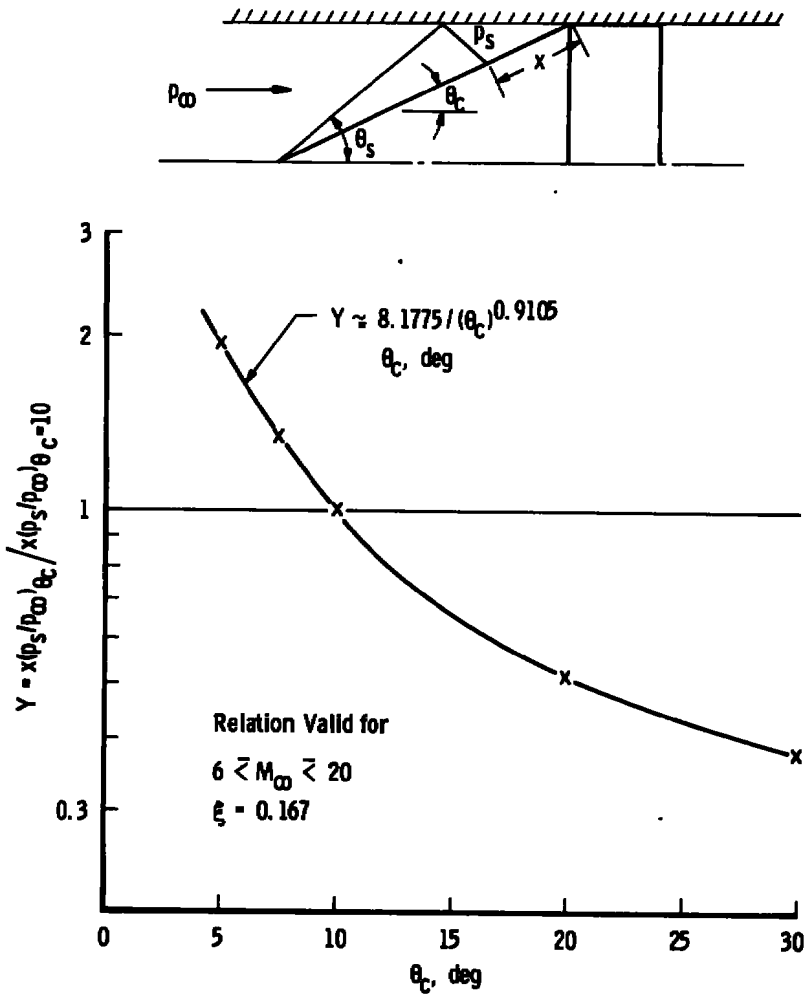
Figure 15. Correction to the parameter K for cone angles other than 10 deg.

A graphical representation for several finite cone angles is shown in Fig. 16. It should be noted that this relationship is still limited to cone nose bluntness values of 0.167. As in all empirical approaches, the degree of confidence decreases as one departs from the original physical model. Additional data are needed in Fig. 16 before great confidence can be placed on the results of the analysis.

Analysis Restricted to Blunt Cones
with $\xi = 0.167$

θ_c, deg

30

20

10

5

30
5
20
10

10-deg Cone Data
$\xi = 0.167$
$15.5 < M_\infty < 19.4$
K from Eq. (7)

——Extrapolation of Data Based on Sharp
Cone Inviscid Flow-Field Analysis
with $C_{D_{SI}} = 0.25\, C_{D_{BL}}$ from Tunnel F Data

K

3.0
1.0
0.10

6   10   14   18   22

M_∞
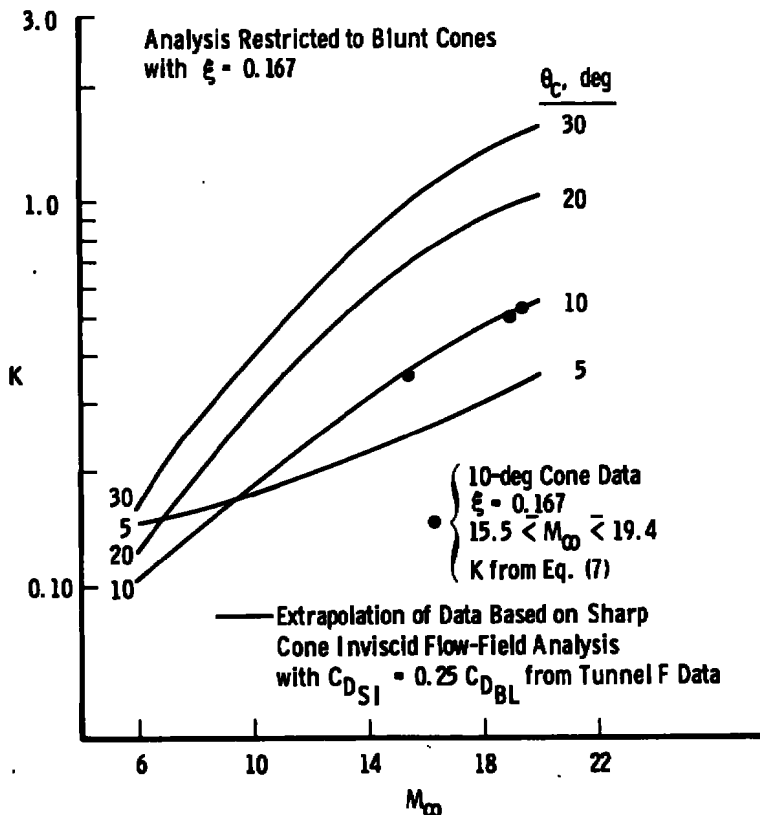
**Figure 16. Graphical representation of the parameter K at
various cone angles and Mach numbers.**

6.1.3 Estimate of the Effect of Nose Bluntness on the Parameter K

By using the present experimental data, the parameter K corrects (in part) the error introduced by assuming a model controlled by sharp cone inviscid flow-field relationships. Since these data were obtained on a blunt cone with $\xi = 0.167$, the previous analysis could not expect to be valid for cone bluntness at values other than 0.167.

Rather tedious hand calculations using the characteristics solutions shown in Fig. 10 and two additional solutions for a 25-deg cone suggest that the variation in the parameter $(x)(p_s/p_\infty)$ as compared to a $\xi = 0.167$ solution, behaves as $\Delta\theta_s^n$ where n is on the order of unity. The ratio of local shock angle θ_s for a blunt cone solution to that of a sharp cone value was calculated and normalized by the value at $\xi = 0.167$. The results for two cone angles (at two Mach numbers) are shown as a function of ξ in Fig. 17. For the

10-deg cone solution the results show a strong function of ξ and a weak function of Mach number in the range from 14 to 20. The solutions for the 25-deg cone were only available for values of $\xi \gtrsim 0.23$. However, at this value, $(\theta_s)_b/(\theta_s)_s$ was very near unity, and it was assumed that the value at $\xi = 0.167$ would also be unity. The numerical effort and time to develop the results shown in Fig. 17 exceeded the effort of all previous results discussed in Section 6. Because of the problems indicated in this figure, the effect of model bluntness discussed later was restricted to

$$\theta_c = 10 \text{ deg}$$

$$0 \lesssim \xi \lesssim 0.3$$

It was also assumed that the results shown in Fig. 17 could be extended from M_∞ = 14 to M_∞ = 6.5, and the parameter K was adjusted from the previous value by multiplying by the relationship, shown in Fig. 17,

$$Z = f(\xi) \tag{10}$$
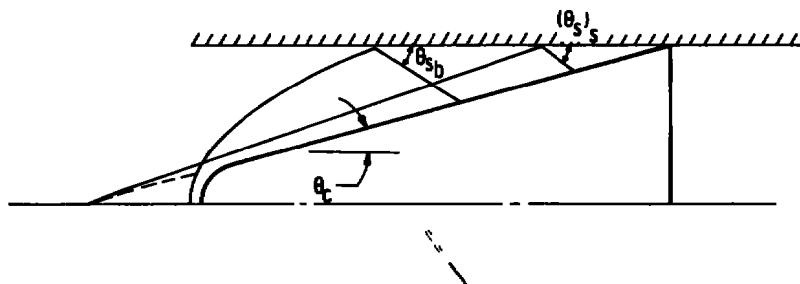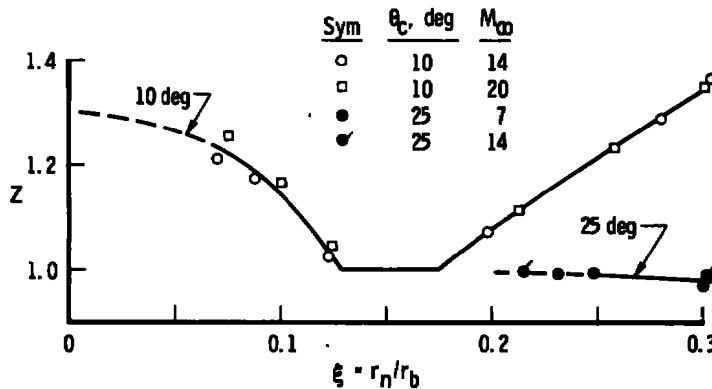
Figure 17. Estimate of the effect of nose bluntness on the parameter K for 10- and 25-deg cones.

This empirical parameter can be expressed,

for $0 \lesssim \xi \lesssim 0.13$,

$$Z \approx 1.3 - 0.26291\ \xi - 5.3788\ \xi^2 - 48.418\ \xi^3 - 248.23\ \xi^4 \tag{11}$$

for $0.13 \lesssim \xi < 0.175$,

$$Z = 1.0 \tag{12}$$

and for $0.175 \lesssim \xi \lesssim 0.30$,

$$Z \simeq 0.52849 + 2.7257\ \xi \tag{13}$$

As is probably evident in the previous discussion, the analysis is basically a rather large extrapolation of a meager amount of data to conditions beyond the combination of model geometry and flow conditions investigated experimentally. A straightforward analysis using blunt body method of characteristics solutions combined with additional experimental data could clarify the situation.

6.2 SLIDING FRICTION DRAG

The mechanism of the forces induced because of sliding friction is beyond the scope of the present analysis. However, it was suggested that the analysis at least include this effect qualitatively, so the term C_{D_F} in Eq. (1) was retained and defined as

$$C_{D_F} = FD/q_\infty A \tag{14}$$

where FD is an arbitrary friction drag expressed in lbf and can be set at any value.

6.3 PRESSURE DRAG

Hopefully, the largest component of drag in Eq. (1) would be inviscid pressure drag, C_{D_P}. In hypersonic flow with sphere cones, Newtonian theory has proven useful in determining this parameter. A closed form solution of axial force is presented in Ref. 13, and for $a = 0$ it can be expressed as

$$C_{D_P} = \frac{C_{P_{max}}}{2}\ \left[\left(1 - \frac{\xi^2}{2}\ \cos^2\theta_c\right)(2\ \sin^2\theta_c) + \xi^2\ \cos^2\theta_c\right] \tag{15}$$

where $C_{P_{max}}$ for Mach numbers greater than 6 has the value $(\gamma + 3)/(\gamma + 1)$. The ratio of specific heats for air (1.4) was used in all calculations of the present analysis. There would be no pressure drag acting on the cylinder portion of the model at $a = 0$.

6.4 SKIN FRICTION DRAG

At the velocities, range pressures, and model sizes proposed for a full-scale track system it is probably correct to assume that the boundary layer will be fully turbulent over a major portion of the model. For a sharp cone, the turbulent skin friction drag referenced to the base area can be expressed by (Ref. 14)

$$C_{D_V} = \frac{0.0776F}{(Re\ell_s)^{0.2}} \left(\frac{V_e}{V_\infty}\right)^{1.8} \left(\frac{p_e}{p_\infty}\right)^{0.8} \left(\frac{T_\infty}{T_e}\right)^{0.58} \left(\frac{H_e}{H*}\right)^{0.58} \cot\theta_c \qquad (16)$$

where

$$\frac{H*}{H_e} = 0.5 + 0.5 \ (T_w/T_\infty) \ (T_\infty/T_e) + 0.0374 \ M_e^2 \qquad (17)$$

The skin friction coefficient decreases with increasing nose radius. However, mass addition caused by ablation greatly reduces the skin friction as determined through the mass addition term, F, in the above equation. Typical variations of F with enthalpy for typical materials are shown in Fig. 18. When Eq. (16) was checked against more recent turbulent boundary-layer solutions available in VKF for several cone geometries and flow conditions, values of C_{D_V} from Eq. (16) from 25 to 40 percent above the VKF solutions
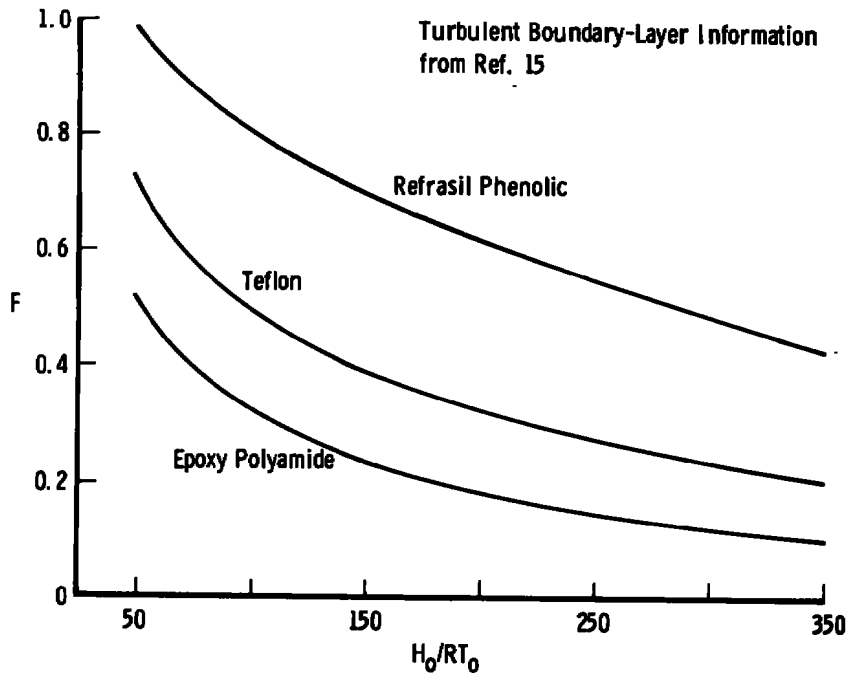
Figure 18. Variation of mass addition term with enthalpy for several ablative materials.

resulted. Equation (16) does not estimate the skin friction component of drag on the cylinder portion of the model. Since this apparent "error" in Eq. (16) is in the positive direction, this contribution to the total skin friction drag would at least be approximated by use of Eq. (16) without modification. It should also be noted that the term C_{D_V} is usually quite small in relation to C_{D_P} or C_{D_T}, so a 25- or 40-percent error in C_{D_V} would not be significant. The stagnation enthalpy term H/RT_o plotted in Fig. 18 should be evaluated using real gas relationships to determine the parameter F in Eq. (16). Its effect is always to reduce the contribution of skin friction to total vehicle drag.

6.5 BASE PRESSURE DRAG

For drag forces defined as in the present case, the contribution of a pressure differential in the model base region to the free-stream value produces a drag component given by

$$C_{D_B} = \frac{2}{\gamma M_\infty^2} \; (1 - p_b/p_\infty) \tag{18}$$

There are numerous data correlations for the ratio of p_b/p_∞. For hypersonic turbulent boundary-layer conditions in the base region of sharp or slightly blunted slender cones, the correlation shown in Fig. 19 can be used. The subscript e refers to local inviscid
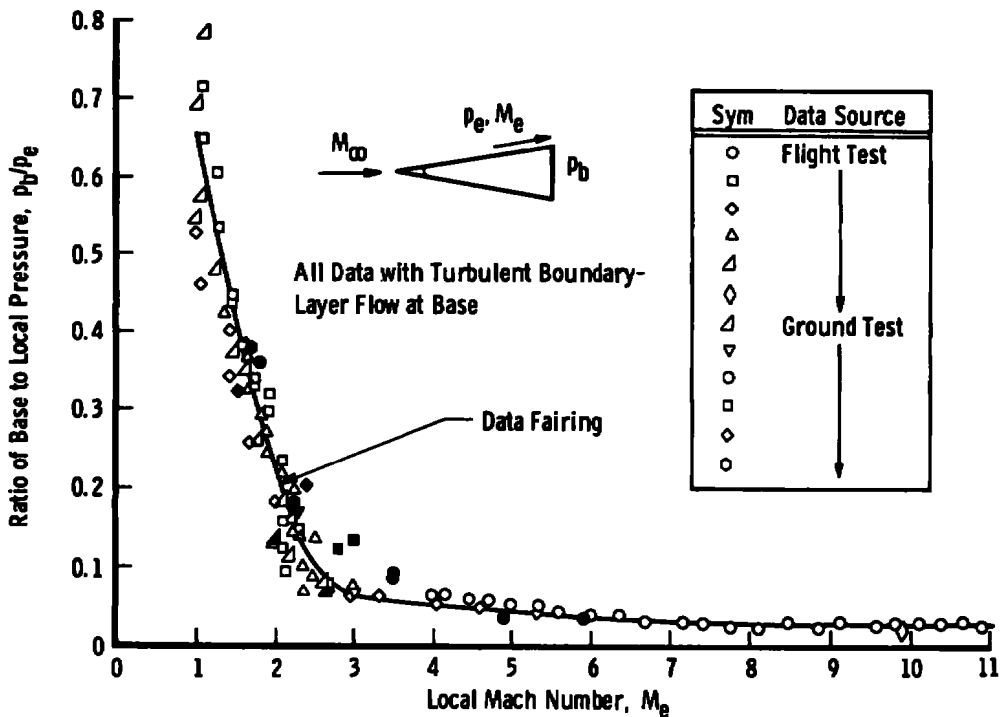
Figure 19. Base pressure data correlation.

edge conditions; therefore, the ratio p_b/p_∞ must be obtained at a given local Mach number by multiplying p_b/p_e from Fig. 19 by a value of p_e/p_∞ obtained from an inviscid flow-field solution for a sharp cone or a characteristics solution for a blunt cone at the end of the conical portion. The present method uses an empirical curve fit for both of these methods in the present range of interest. It should be noted that Eq. (18) neglects any effect of the expansion around the corner of the cone to the cylindrical portion of the model and also neglects the influence of the track on the average pressure in the base region. This problem is amenable to experimental study. For certain large cone angles, Eq. (18) will predict a negative base drag component (thrust). This occurs, however, only when forebody pressure drag is quite large.

6.6 INDUCED PRESSURE DRAG

At turbulent boundary-layer conditions, the effect of viscous-induced pressure drag on total vehicle drag is usually less than one percent. For this reason, induced pressure drag is neglected in the present analysis.

7.0 RESULTS OF THE ANALYSIS AND CONCLUSIONS

The relationships derived and discussed in Section 6.0 were programmed, with the necessary auxiliary relationships, for the AEDC-IBM 360/370 computer. Parametric studies of the different variables were then conducted. Input information required, and corresponding empirical limits, were as follows. All calculations were performed for a range ambient temperature of 300°K.

Model velocity, fps, $7{,}410 \lesssim V_\infty \lesssim 28{,}475$

Range pressure, torr, no limits

Track diameter, in., no limits

Track rail width, in., no limits

Cone half-angle, deg, $5 \lesssim \theta_c \lesssim 30$

$\xi \begin{cases} 0 \lesssim \xi \lesssim 0.3 \text{ for } \theta_c = 10 \text{ deg} \\ \xi = 0.167 \text{ for } \theta_c \neq 10 \text{ deg} \end{cases}$

Model weight, lbm, no limits

Friction drag, lbf, no limits

Model wall temperature, °K, no limits

Mass fraction, $0 \lesssim F \lesssim 1.0$

With this information, the program calculates the necessary free-stream conditions and each component of drag in Eq. (1). Also, the ballistic coefficient is calculated using the expression

$$B = W/C_{D_T} A \qquad (19)$$

An extremely large number of combinations of input variables could be devised from the information listed above. Only a few were examined, and the results are discussed below.

The effect of model wall temperature on the term C_{D_V} [Eq. (16)] and total drag, C_{D_T} [Eq. (1)], was studied for a 10-deg cone at model velocity of 20,000 fps. The effect of varying wall temperature from 300 to 3000°K on the term $C_{D_{SI}}/C_{D_T}$ was only about 2 percent. All subsequent calculations were therefore performed for a wall temperature of 811°K (1000°F). A similar small effect of the mass fraction parameter, F[Eq. (16)], was also noted, and subsequent calculations were performed for a nonablating model (F = 1.0).

The majority of the remaining calculations to be discussed were performed for a 10-deg, slightly blunted cone with ξ = 0.167. This model corresponds to the available experimental data and results in the greatest confidence in the parameter K (Section 6.0). Track diameter, TD, was arbitrarily chosen for most solutions at 10.0 in. and rail width, RW, was scaled directly from the present experimental apparatus (Fig. 1) with a resulting value of 2.308 in. Unless otherwise indicated, all solutions assume zero friction between model and rail.

The contribution of shock interaction drag, expressed as $C_{D_{SI}}/C_{D_T}$, as a function of model velocity and range pressure is shown in Fig. 20. A very strong influence of model velocity and a weaker dependence on range pressure is shown for this model and track configuration. Increase in total drag due to model bow shock interaction varies from about 9 percent to as much as 30 percent of the total deceleration force of the model over the range of velocities and pressures shown. The same information is shown in a different format in Fig. 21. In order to calculate the ballistic coefficient, B, model weight is required. All solutions shown in Fig. 21 use a model weight of 65 lbm. This represents the present estimated launcher limit for a 10.0-in.-diam, two-stage light gas gun at a launch velocity of 20,000 fps. Although the lower velocities shown in Fig. 21 could have used a higher model mass, the solutions retained a value of 65 lbm to prevent the introduction of another variable. Subsequent calculations for launchers of diameters other than 10 in. and launch velocities other than 20,000 fps often use the maximum model weight for a given combination of diameter and velocity calculated from the empirical relationship

$$W_{max} = 65 \left(\frac{TD}{10}\right)^3 (20,000)^2/(V_\infty)^2 \qquad (20)$$

37
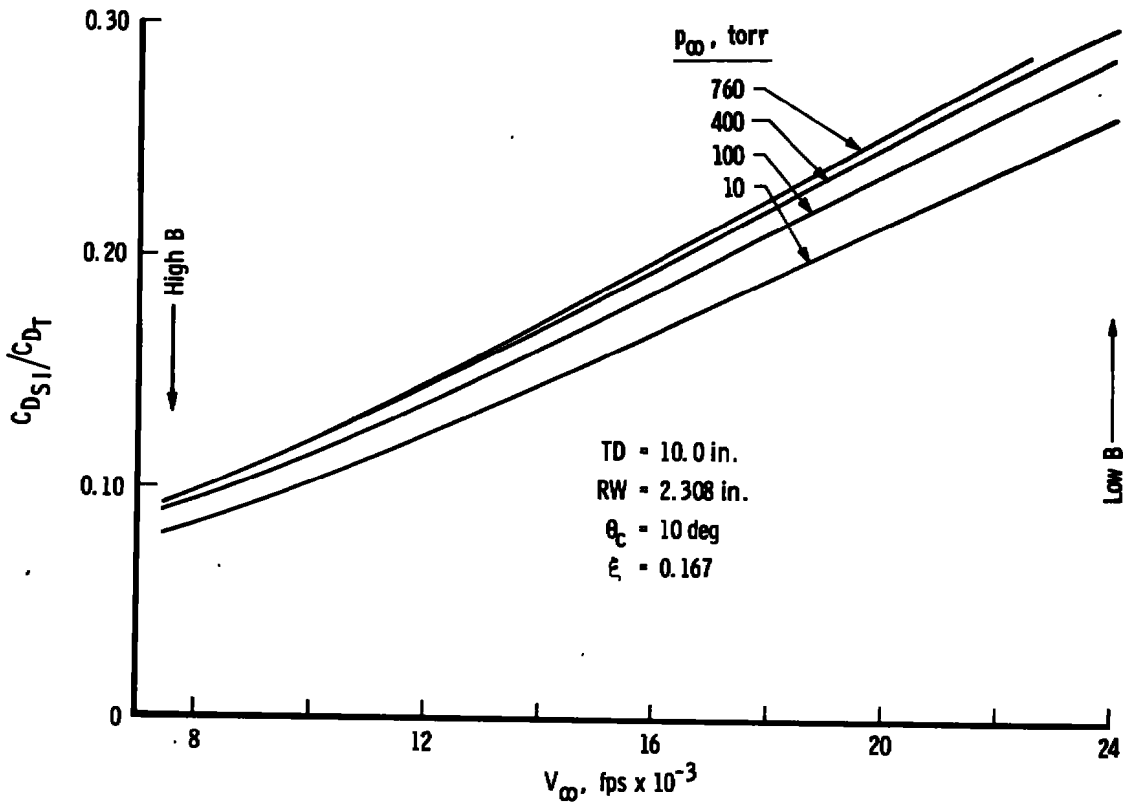
Figure 20. Effect of velocity and pressure on shock interaction drag.
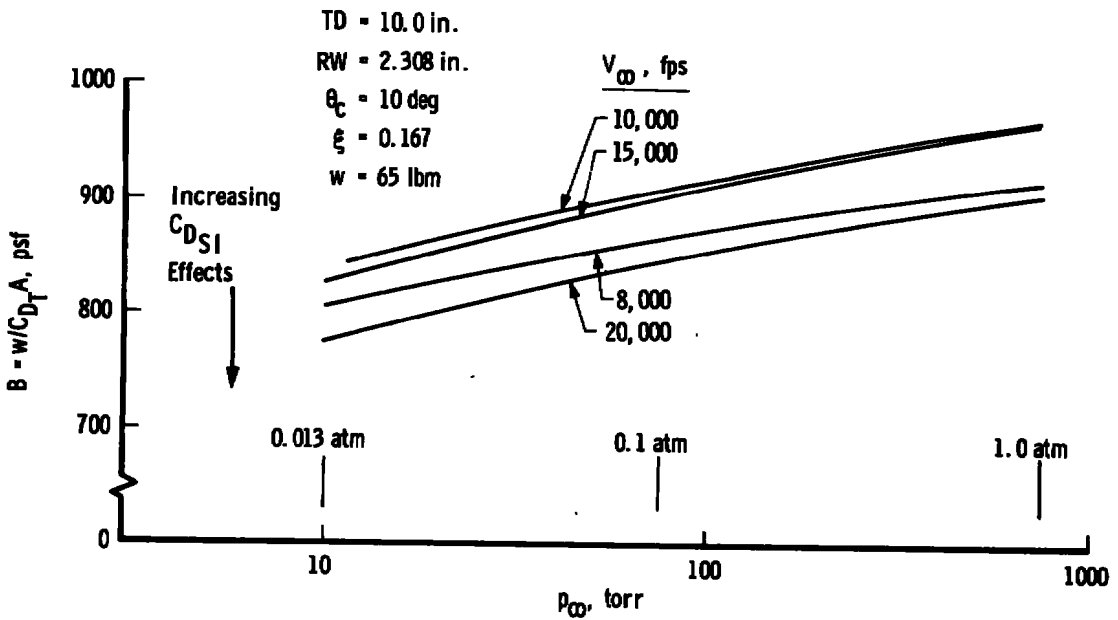
Figure 21. Effect of velocity and pressure on ballistic coefficient.

where W_{max} is in pounds mass, TD is in inches, and V_{∞} is in feet per second. The ballistic coefficient varied from as low as 775 to as high as 970·lbm/ft² over the range of range pressures and model velocities shown. The nonlinear influence of model velocity should be noted. The optimum velocity was 10,000 fps, with lower ballistic coefficients resulting for both higher and lower model velocities. This was probably due to the fact that, for this model, the term $C_{D_{SI}}$ was close to the term C_{D_V} in Eq. (1). For a given velocity, the relative effect of range pressure is shown to decrease as it increases toward one atmosphere.

The effect of model bluntness ratio and velocity on shock interaction drag on a 10-deg cone is shown in Fig. 22. The calculations were performed for a constant range pressure of 100 torr. A very large influence of both bluntness ratio and velocity can be seen to exist with the contribution of model bow shock increasing to greater than 40 percent of the total drag as the model becomes sharp and velocity increases to 24,000 fps. A more realistic upper velocity would be 20,000 fps. The effect of range pressure and model bluntness is shown in Fig. 23 for this velocity. Comparing Figs. 22 and 23
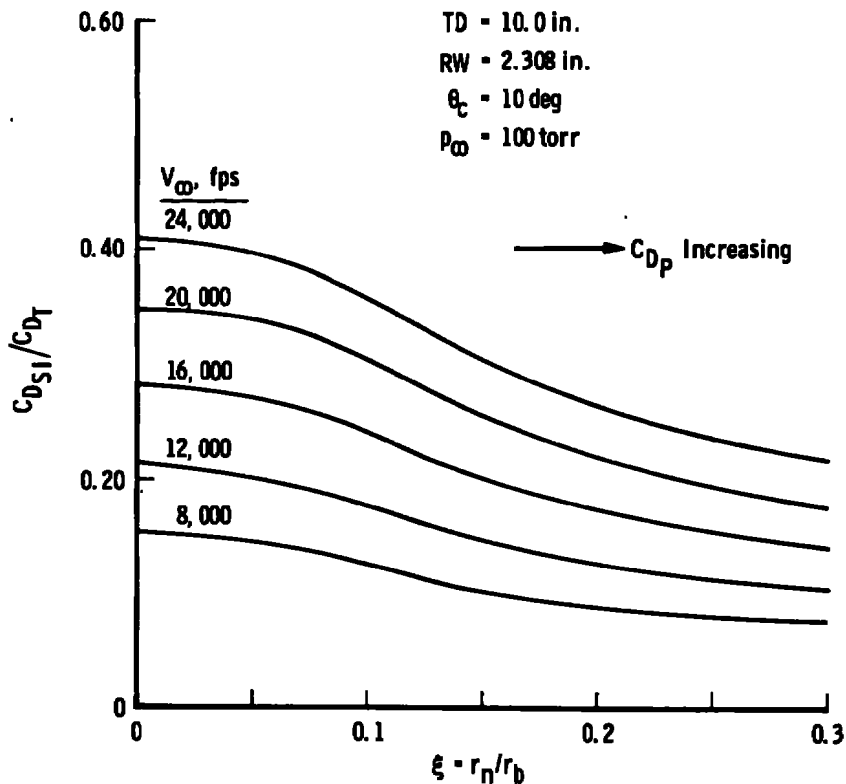
Figure 22. Effect of bluntness ratio and velocity on 10-deg cone shock interaction drag.

indicates the relative influence of model velocity and range pressure at a given bluntness ratio. It should be noted that the term $C_{D_{SI}}/C_{D_T}$ becomes smaller as ξ increases because of a large increase in the pressure drag term, C_{D_p}, in Eq. (1) and not because of a decrease in shock interaction drag, $C_{D_{SI}}$.
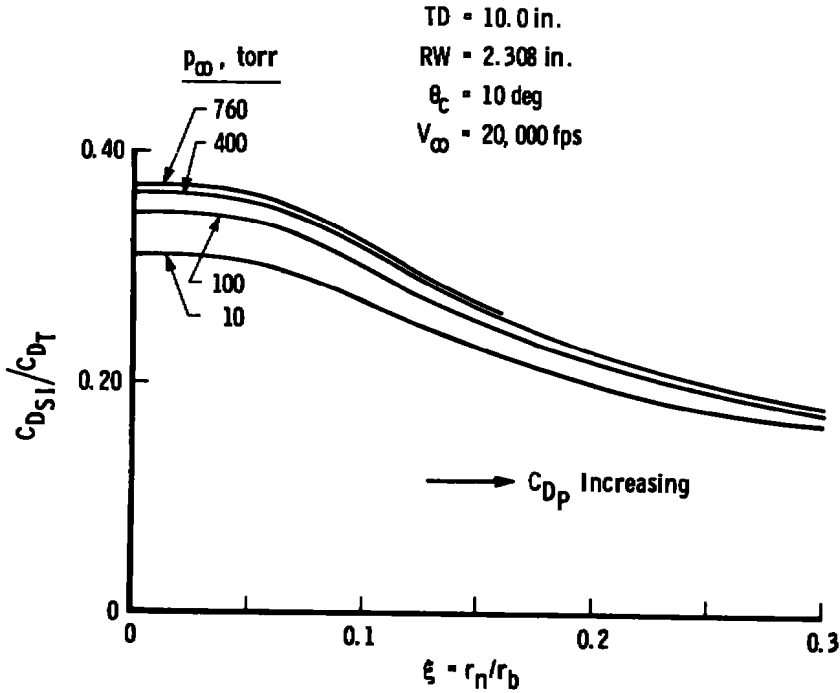
Figure 23. Effect of bluntness ratio and range pressure on 10-deg cone shock interaction drag.

The effect of track diameter on shock interaction drag for 10-deg models of constant nose radius is shown in Fig. 24. These solutions were run for a model velocity of 20,000 fps and a range pressure of 100 torr. It was necessary to vary nose bluntness ratio, ξ, from 0.036 to 0.250 to produce these solutions. Rail width was increased or decreased in direct proportion to track diameter with the value of 2.308 in. being retained for the 10.0-in. track diameter. It is seen that, for a given nose radius, the effect of increasing track diameter is small, but for a given track diameter. decreasing nose radius results in a greater contribution of shock interaction drag as a percent of total model drag. This latter conclusion was also obtained from Figs. 22 and 23 and again results from the increase in C_{D_p} rather than from a decrease in $C_{D_{SI}}$ as nose radius increases.

All previous solutions have utilized a model with a cone angle of 10 deg. The effect of varying cone angle and model velocity on shock interaction drag in terms of $C_{D_{SI}}/C_{D_T}$ is shown in Fig. 25. All of these solutions were performed for a bluntness ratio, ξ, of
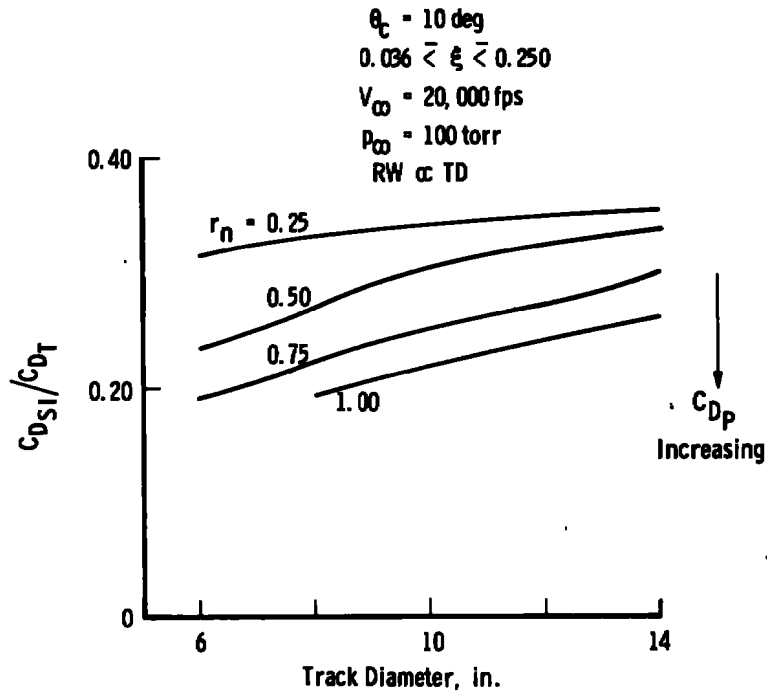
Figure 24. Shock interaction drag as a function of track diameter
with constant nose radii.
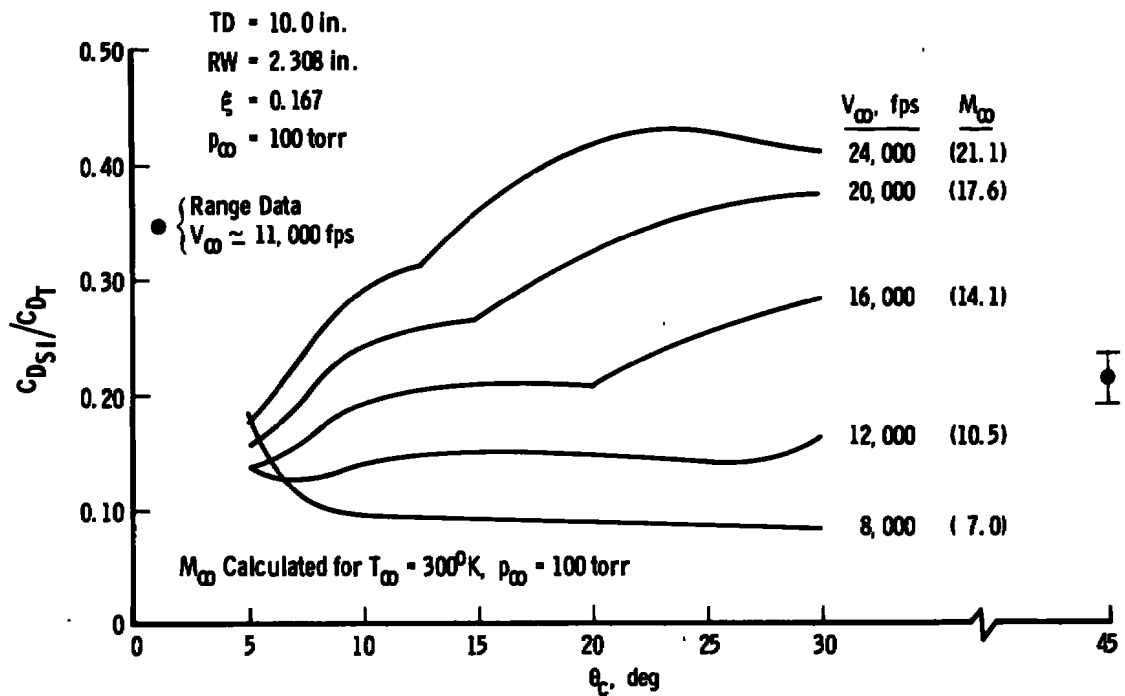
Figure 25. Effect of cone angle and velocity on shock interaction drag.

0.167 and a track diameter of 10.0 in., with a rail width of 2.308 in. Range pressure was held at 100 torr. A most unusual behavior with increasing cone angle is seen for several velocity values. A combination of high velocity and cone angle results in shock interaction drag being greater than 40 percent of the total vehicle drag. Conversely, for small cone angles, the effect of velocity is quite small, with the shock interaction drag component being only about 14 to 18 percent of the total drag. The Mach number values listed with the velocity values in Fig. 25 are for a free-stream (range) temperature of 300°K as well as a free-stream pressure of 100 torr. As a matter of interest, range measurements obtained by the McDonnell Douglas Corporation on a 45-deg sharp cone-cylinder model (Ref. 1) are also shown in Fig. 25. Although these data are in qualitative agreement with the present analysis, this may be fortuitous since the shock mechanism is completely different from that presently assumed (Figs. 7 and 9), and the track data may have included rail friction forces, which are not considered in Fig. 25.

The procedure of directly scaling rail width to track diameter from the values shown in Fig. 1 to larger track diameters was somewhat arbitary. Other design considerations may require that rail width be scaled by a factor other than unity. From a viewpoint of shock interaction drag, it would be advantageous if the scaling constant were less than unity. This is shown graphically in Fig. 26. The influence of rail width in terms of the
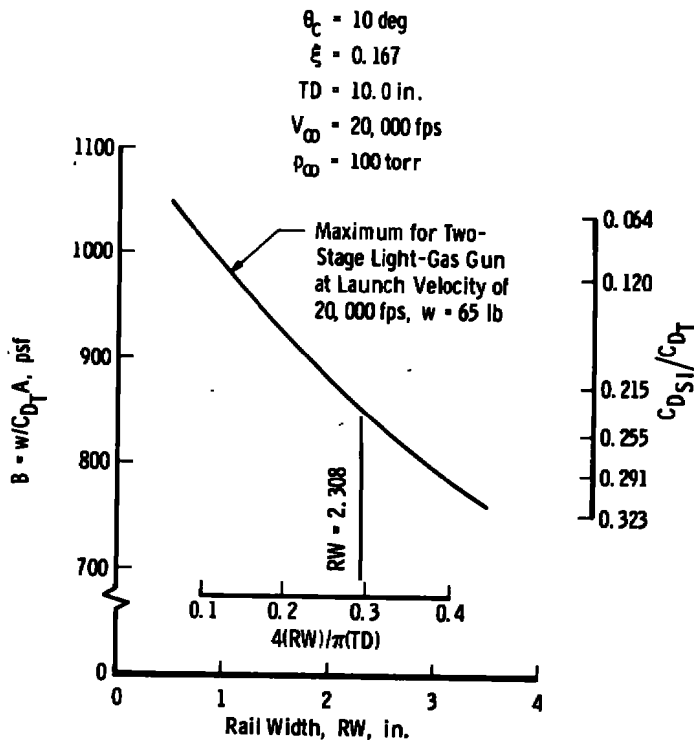
Figure 26. Effect of rail width on maximum ballistic coefficient and shock interaction drag.

parameter $C_{D_{SI}}/C_{D_T}$ and ballistic coefficient are both shown. The calculations were performed for a 10.0-in. track with a 10-deg cone of bluntness ratio 0.167 at a velocity of 20,000 fps and range pressure of 100 torr. Present two-stage light-gas gun development suggests that future systems of 10-in. diameter launching a model at 20,000 fps would be limited to a model weight no greater than 65 lbm. This value would yield the greatest ballistic coefficient and is the value used in the calculation shown in Fig. 26. The parameter $4(RW)/\pi(TD)$ (ratio of total rail width to track circumference) is also indicated in Fig. 26. This parameter is utilized later in graphical and tabular presentations. A very large reduction in the shock interaction drag in terms of total drag and available ballistic coefficient is observed as rail width is decreased.

All previous solutions have been obtained with the assumption of zero sliding friction between the cylinder portion of the model and the track rail. This was done because the present experimental program was designed only to study shock interaction and no accurate estimate has as yet been made on the sliding friction term (C_{D_F}) in Eq. (1). Track curvature, nonsymmetric ablation, model weight, and materials all influence friction as well as model velocity. From Eq. (1), total "track-related" drag force would be $C_{D_{SI}}$ plus C_{D_F}. This parameter in terms of C_{D_T} and the previous parameter $C_{D_{SI}}/C_{D_T}$ is shown as a function of absolute track friction drag in Fig. 27. The solutions were obtained at velocities of 8,000 and 20,000 fps, with other input information tabulated in the figure. Since the friction force is included in C_{D_T} [Eq. (1)], the parameter $C_{D_{SI}}/C_{D_T}$ decreases with increasing track friction drag. The parameter $(C_{D_{SI}} + C_{D_F})/C_{D_T}$ is seen to increase much faster for the lower velocity case than for the higher velocity value. For an arbitrary
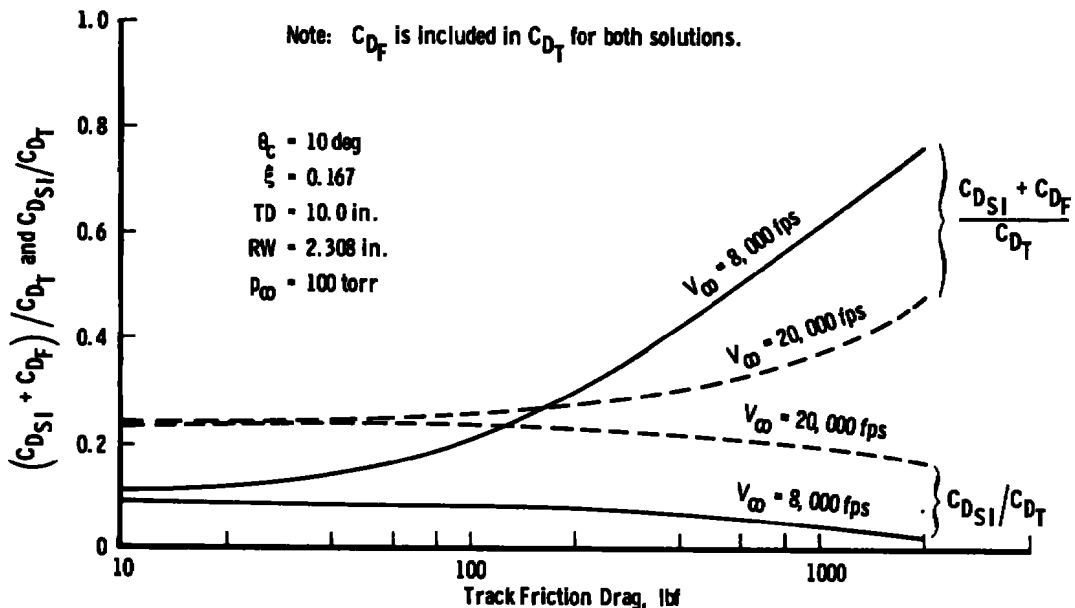
Figure 27. Effect of friction drag at two velocities.

track friction of 2000 lbf at a velocity of 8000 fps, the total track-related deceleration force represents about 76 percent of the total vehicle drag for the model configuration indicated in Fig. 27. Although this is a rather severe penalty, the actual friction force would probably be much less than 2000 pounds at this velocity and the penalty quickly becomes smaller as friction is decreased. A more realistic estimate of the relative magnitude of shock interaction and track friction drag is shown in Fig. 28. For lower velocities and friction, friction-related drag is small compared to shock interaction drag and increases to about the same magnitude at higher velocities and absolute friction forces. The extreme slope of the parameter $C_{D_F}/C_{D_{SI}}$ in Fig. 28 suggests the need for better definition of these expected track friction forces. All additional calculations discussed herein assume zero friction.
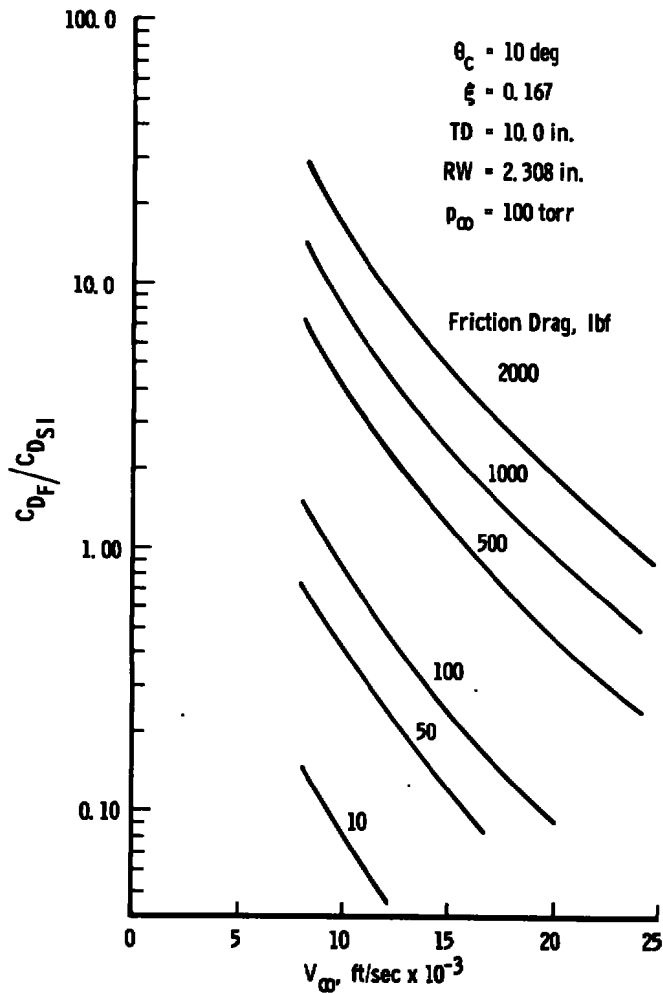
Figure 28. Ratio of friction to shock interaction drag as a function of velocity.

Planning plots for four typical model geometries and range conditions are shown in Fig. 29. The solutions are shown as ballistic coefficients as a function of model weight and track diameter. Also shown is the present estimated limit for launch weights of two-stage light-gas guns. With this as the maximum available ballistic coefficient, the summary plot shown in Fig. 30 was prepared. The penalty for shock interaction drag ranged from about 14 to 43 percent for these cases. The advantage of increasing track diameter in obtaining greater ballistic coefficients can be seen. It should also be remembered that track friction forces are assumed to be zero for these calculations.

A slightly different type of planning plot is shown in Fig. 31. To minimize the total number of variables, all these solutions were obtained for a model velocity of 18,000 fps, but model weights were calculated for launch velocities of 17,000 and 20,000 fps over the launcher diameter (track diameter) range indicated on the figure. As can be seen in Fig. 25, the error involved in using a model weight calculated for a launch velocity of 17,000 fps and then "flown" at 18,000 fps (for a 5- or 10-deg cone) is not large. Model cone angles of 5 and 10 deg represent typical full-scale reentry vehicle (RV) values which might be fired in a full-scale ablation range facility. As expected, available ballistic coefficient is a strong function of track diameter and a weaker function of rail width. Maximum available ballistic coefficient varies from about 500 to greater than 4000.
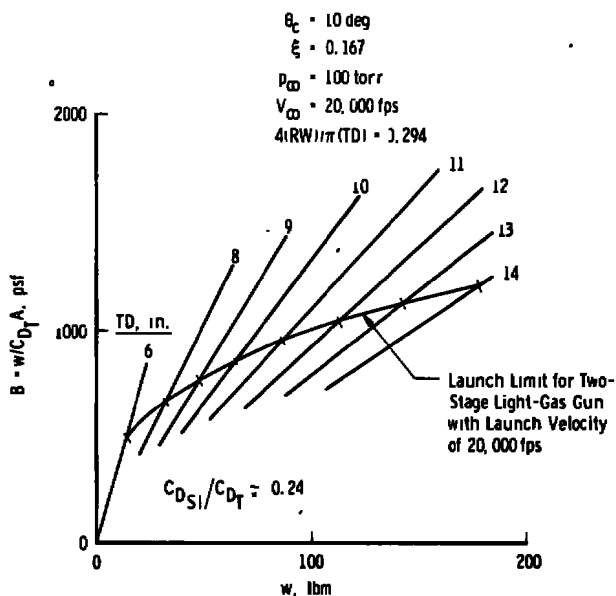
a. θ_c = 10 deg, V_∞ = 20,000 fps

Figure 29. Planning plot for four typical model geometries and range conditions.
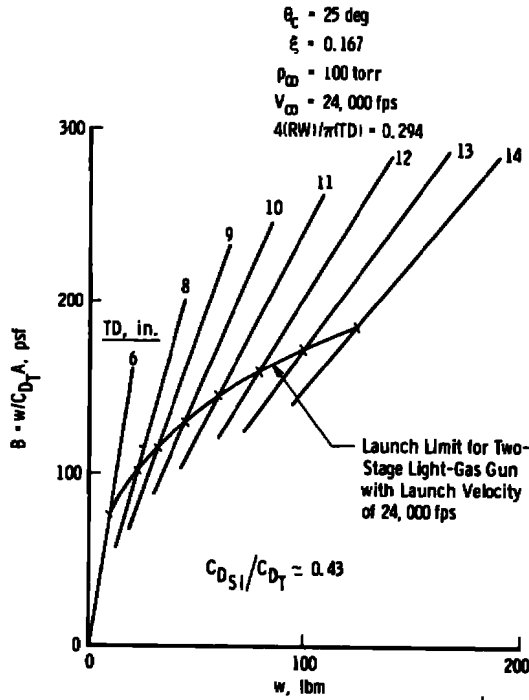
b. $\theta_c = 25$ deg, $V_\infty = 24,000$ fps
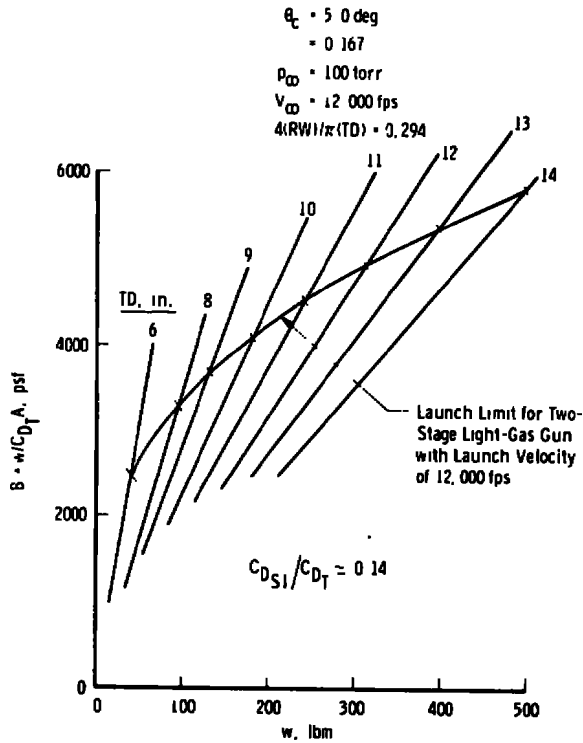
c. $\theta_c = 5$ deg, $V_\infty = 12,000$ fps
Figure 29. Continued.

θ_c = 10.0 deg
ξ = 0
p_∞ = 760 torr
V_∞ = 20,000 fps
4(RW)/π(TD) = 0.294

2000

TD, in.
6
8
9
10
11
12
13
14

B = w/C_{D_T}A, psf

1000

Launch Limit for Two-
Stage Light-Gas Gun
with Launch Velocity
of 20,000 fps

$C_{D_{SI}}/C_{D_T} \cong 0.37$

0

0   100   200

w, lbm
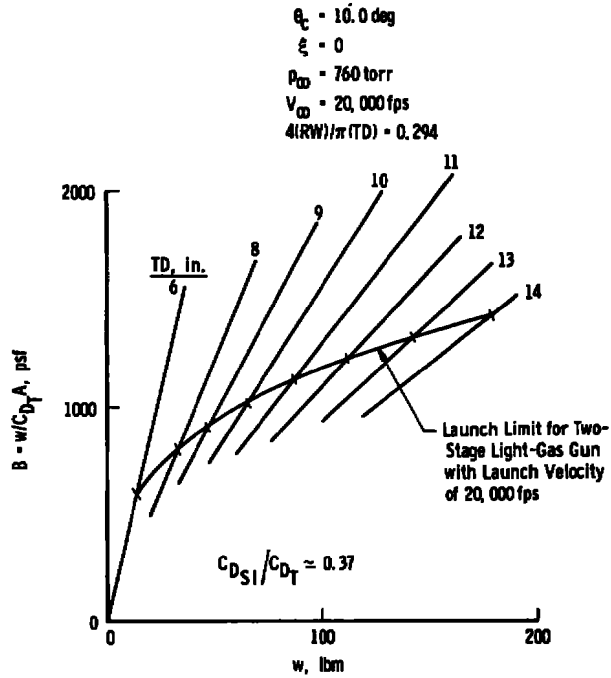
d. θ_c = 1U deg, V_∞ = 20,000 fps
Figure 29. Concluded.

5000

C

1000

D
A

500

B = w/C_{D_T}A, psf

Curve	θ_c, deg	ξ	Launch Velocity, fps	p_∞, torr	$C_{D_{SI}}/C_{D_T}$
A	10	0.167	20,000	100	~0.24
B	25	0.167	24,000	100	~0.43
C	5	0.167	12,000	100	~0.14
D	10	0	20,000	760	~0.37

100

B

50

6   10   14

TD, in.
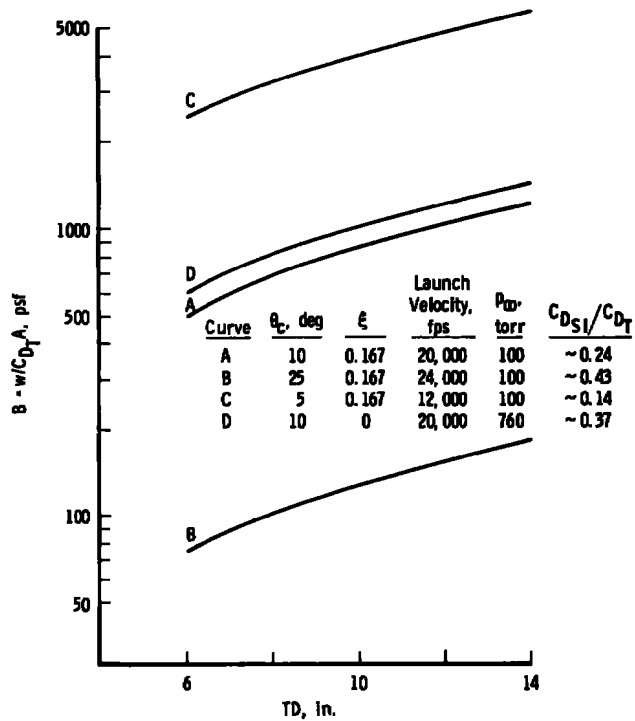
Figure 30. Summary of available ballistic coefficient
for four cases.

47

The two extreme values (minimum and maximum B) in Fig. 31 were chosen to perform trajectory calculations,* and the results are shown in Fig. 32. These trajectory solutions utilize an aerodynamic drag curve as a function of velocity calculated from Eq. (1), and in addition, Eq. (1) was solved with the term $C_{D_{SI}}$ set equal to zero (no shock interaction). The trajectory solutions were run for a time interval sufficient to allow
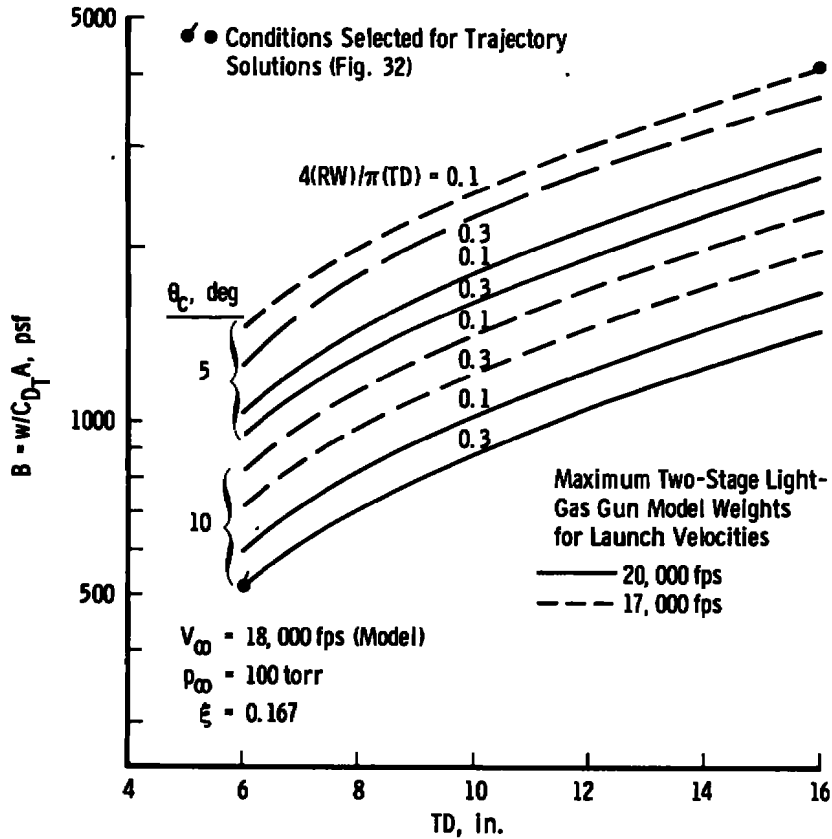
Figure 31. Planning case with zero friction forces.

a full-scale range distance of 50,000 ft to be traversed. The resulting ballistic coefficient as a function of range length is shown in Fig. 32a, and model velocities are shown in Fig. 32b. For these models, track dimension, and range conditions. the penalty for utilizing a constraining track is no greater than 13 percent in terms of ballistic coefficient and 1300 fps in terms of reduced model velocity. These solutions were run assuming no sliding friction forces were present between the model cylinder and rail surface.

---

*Trajectory solutions were obtained by J. P. Billingsley, VKF/ADP.
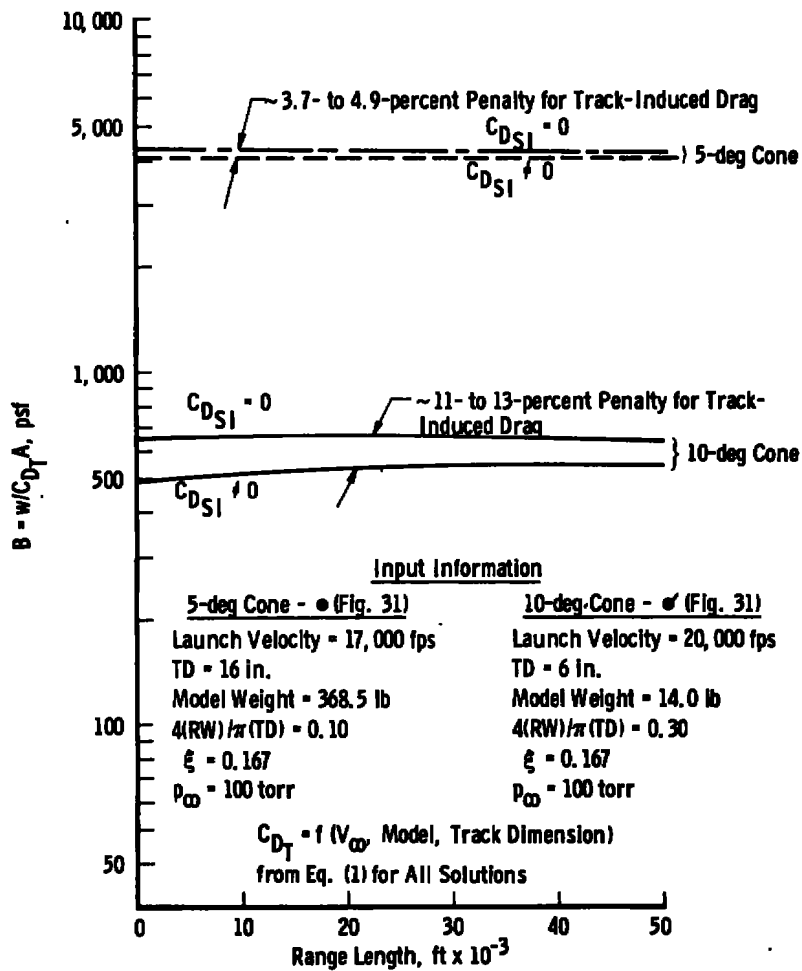
a. Ballistic coefficient
Figure 32. Results of trajectory solutions.

Finally, an additional set of solutions is shown in tabular format in Table 5. Initial conditions and table nomenclature are as follows:

Input Data

V_∞ = UINF = 12,000, 16,000, 20,000, and 24,000 fps

p_∞ = PINF = 10, 100, and 1000 torr

θ_c = THETAC = 5.0, 7.5, and 10.0 deg

ξ = RN/RB = 0.167 for θ_c = 5.0 and 7.5 deg

= 0, 0.10, 0.167, 0.2, and 0.3 for θ_c = 10 deg

4(RW)/(TD) = RAIL/CIR = 0.1, 0.2, 0.3, and 0.4

Output Data

$$C_{D_P} + C_{D_V} + C_{D_B} = CDAERO$$

$$C_{D_{SI}} = CDSI$$

$$C_{D_T} = CDT$$

$$C_{D_{SI}}/C_{D_T} = CDSI/CDT$$
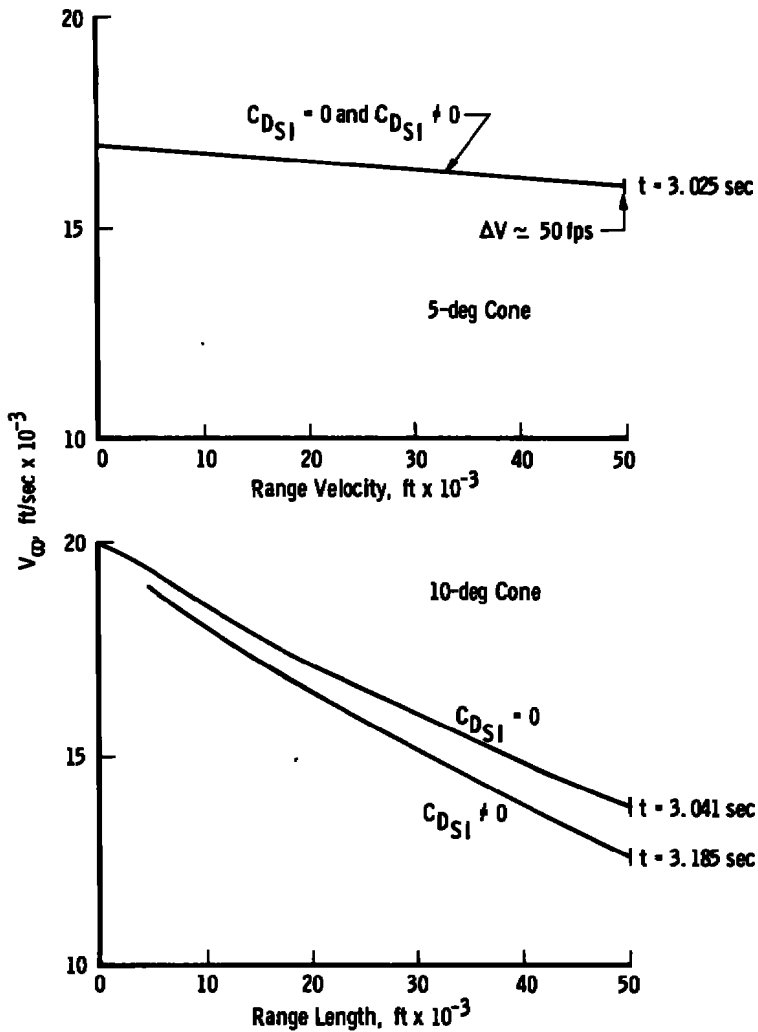
b. Velocity
Figure 32. Concluded.

Table 5. Shock Interaction Drag for Aeroballistic Track Systems

UINF FPS	PINF TORR	THETAC DEG.	RN/RB	HAIL/CIR	CDAERO	CDSI	CDT	CDSI/CDT
12000.0	10.00	5.0	0.167	0.10	0.0807	0.0038	0.0845	0.0449
12000.0	10.00	5.0	0.167	0.20	0.0807	0.0076	0.0883	0.0860
12000.0	10.00	5.0	0.167	0.30	0.0807	0.0114	0.0921	0.1236
12000.0	10.00	5.0	0.167	0.40	0.0807	0.0152	0.0959	0.1583
16000.0	10.00	5.0	0.167	0.10	0.0744	0.0035	0.0779	0.0453
16000.0	10.00	5.0	0.167	0.20	0.0744	0.0071	0.0814	0.0867
16000.0	10.00	5.0	0.167	0.30	0.0744	0.0106	0.0850	0.1247
16000.0	10.00	5.0	0.167	0.40	0.0744	0.0141	0.0885	0.1596
20000.0	10.00	5.0	0.167	0.10	0.0716	0.0039	0.0754	0.0511
20000.0	10.00	5.0	0.167	0.20	0.0716	0.0077	0.0793	0.0974
20000.0	10.00	5.0	0.167	0.30	0.0716	0.0116	0.0831	0.1392
20000.0	10.00	5.0	0.167	0.40	0.0716	0.0154	0.0870	0.1775
24000.0	10.00	5.0	0.167	0.10	0.0702	0.0044	0.0747	0.0596
24000.0	10.00	5.0	0.167	0.30	0.0702	0.0134	0.0836	0.1597
24000.0	10.00	5.0	0.167	0.40	0.0702	0.0178	0.0880	0.2022
12000.0	100.00	5.0	0.167	0.10	0.0698	0.0038	0.0736	0.0515
12000.0	100.00	5.0	0.167	0.20	0.0698	0.0076	0.0774	0.0981
12000.0	100.00	5.0	0.167	0.30	0.0698	0.0114	0.0812	0.1402
12000.0	100.00	5.0	0.167	0.40	0.0698	0.0152	0.0850	0.1787
16000.0	100.00	5.0	0.167	0.10	0.0639	0.0035	0.0674	0.0524
16000.0	100.00	5.0	0.167	0.20	0.0639	0.0071	0.0709	0.0996
16000.0	100.00	5.0	0.167	0.30	0.0639	0.0106	0.0745	0.1423
16000.0	100.00	5.0	0.167	0.40	0.0639	0.0141	0.0780	0.1812
20000.0	100.00	5.0	0.167	0.10	0.0612	0.0039	0.0651	0.0593
20000.0	100.00	5.0	0.167	0.20	0.0612	0.0077	0.0689	0.1120
20000.0	100.00	5.0	0.167	0.30	0.0612	0.0116	0.0728	0.1591
20000.0	100.00	5.0	0.167	0.40	0.0612	0.0154	0.0766	0.2015
24000.0	100.00	5.0	0.167	0.10	0.0599	0.0044	0.0643	0.0691
24000.0	100.00	5.0	0.167	0.20	0.0599	0.0089	0.0688	0.1294
24000.0	100.00	5.0	0.167	0.30	0.0599	0.0134	0.0732	0.1823
24000.0	100.00	5.0	0.167	0.40	0.0599	0.0178	0.0777	0.2292
12000.0	1000.00	5.0	0.167	0.10	0.0629	0.0038	0.0667	0.0569
12000.0	1000.00	5.0	0.167	0.20	0.0629	0.0076	0.0705	0.1077
12000.0	1000.00	5.0	0.167	0.30	0.0629	0.0114	0.0743	0.1532
12000.0	1000.00	5.0	0.167	0.40	0.0629	0.0152	0.0781	0.1944
16000.0	1000.00	5.0	0.167	0.10	0.0572	0.0035	0.0608	0.0581
16000.0	1000.00	5.0	0.167	0.20	0.0572	0.0071	0.0643	0.1099
16000.0	1000.00	5.0	0.167	0.30	0.0572	0.0106	0.0678	0.1562
16000.0	1000.00	5.0	0.167	0.40	0.0572	0.0141	0.0714	0.1980
20000.0	1000.00	5.0	0.167	0.10	0.0547	0.0039	0.0585	0.0659
20000.0	1000.00	5.0	0.167	0.20	0.0547	0.0077	0.0624	0.1238
20000.0	1000.00	5.0	0.167	0.30	0.0547	0.0116	0.0662	0.1748
20000.0	1000.00	5.0	0.167	0.40	0.0547	0.0154	0.0701	0.2203
24000.0	1000.00	5.0	0.167	0.10	0.0534	0.0044	0.0578	0.0770
24000.0	1000.00	5.0	0.167	0.20	0.0534	0.0089	0.0623	0.1430
24000.0	1000.00	5.0	0.167	0.30	0.0534	0.0134	0.0667	0.2002
24000.0	1000.00	5.0	0.167	0.40	0.0534	0.0178	0.0712	0.2502

Table 5. Continued

UINF FPS	PINF TORR	THETAC DEG.	RN/RB	RAIL/CLR	CDAERO	CDSI	CDT	CDSI/CDT
12000.0	10.00	7.5	0.167	0.10	0.0984	0.0042	0.1026	0.0414
12000.0	10.00	7.5	0.167	0.20	0.0984	0.0085	0.1069	0.0795
12000.0	10.00	7.5	0.167	0.30	0.0984	0.0127	0.1111	0.1147
12000.0	10.00	7.5	0.167	0.40	0.0984	0.0170	0.1154	0.1474
16000.0	10.00	7.5	0.167	0.10	0.0944	0.0053	0.0997	0.0532
16000.0	10.00	7.5	0.167	0.20	0.0944	0.0106	0.1050	0.1011
16000.0	10.00	7.5	0.167	0.30	0.0944	0.0159	0.1103	0.1444
16000.0	10.00	7.5	0.167	0.40	0.0944	0.0212	0.1156	0.1837
20000.0	10.00	7.5	0.167	0.10	0.0931	0.0068	0.0999	0.0680
20000.0	10.00	7.5	0.167	0.20	0.0931	0.0136	0.1067	0.1274
20000.0	10.00	7.5	0.167	0.30	0.0931	0.0204	0.1135	0.1796
20000.0	10.00	7.5	0.167	0.40	0.0931	0.0272	0.1203	0.2260
24000.0	10.00	7.5	0.167	0.10	0.0929	0.0085	0.1014	0.0841
24000.0	10.00	7.5	0.167	0.20	0.0929	0.0171	0.1099	0.1553
24000.0	10.00	7.5	0.167	0.30	0.0929	0.0256	0.1185	0.2161
24000.0	10.00	7.5	0.167	0.40	0.0929	0.0341	0.1270	0.2689
12000.0	100.00	7.5	0.167	0.10	0.0869	0.0042	0.0911	0.0466
12000.0	100.00	7.5	0.167	0.20	0.0869	0.0085	0.0954	0.0891
12000.0	100.00	7.5	0.167	0.30	0.0869	0.0127	0.0996	0.1280
12000.0	100.00	7.5	0.167	0.40	0.0869	0.0170	0.1039	0.1637
16000.0	100.00	7.5	0.167	0.10	0.0824	0.0053	0.0878	0.0605
16000.0	100.00	7.5	0.167	0.20	0.0824	0.0106	0.0931	0.1141
16000.0	100.00	7.5	0.167	0.30	0.0824	0.0159	0.0984	0.1619
16000.0	100.00	7.5	0.167	0.40	0.0824	0.0212	0.1037	0.2048
20000.0	100.00	7.5	0.167	0.10	0.0808	0.0068	0.0876	0.0776
20000.0	100.00	7.5	0.167	0.20	0.0808	0.0136	0.0944	0.1440
20000.0	100.00	7.5	0.167	0.30	0.0808	0.0204	0.1012	0.2015
20000.0	100.00	7.5	0.167	0.40	0.0808	0.0272	0.1080	0.2518
24000.0	100.00	7.5	0.167	0.10	0.0802	0.0085	0.0887	0.0962
24000.0	100.00	7.5	0.167	0.20	0.0802	0.0171	0.0972	0.1756
24000.0	100.00	7.5	0.167	0.30	0.0802	0.0256	0.1058	0.2421
24000.0	100.00	7.5	0.167	0.40	0.0802	0.0341	0.1143	0.2987
12000.0	1000.00	7.5	0.167	0.10	0.0796	0.0042	0.0839	0.0507
12000.0	1000.00	7.5	0.167	0.20	0.0796	0.0085	0.0881	0.0965
12000.0	1000.00	7.5	0.167	0.30	0.0796	0.0127	0.0924	0.1380
12000.0	1000.00	7.5	0.167	0.40	0.0796	0.0170	0.0966	0.1760
16000.0	1000.00	7.5	0.167	0.10	0.0749	0.0053	0.0802	0.0661
16000.0	1000.00	7.5	0.167	0.20	0.0749	0.0106	0.0855	0.1241
16000.0	1000.00	7.5	0.167	0.30	0.0749	0.0159	0.0908	0.1753
16000.0	1000.00	7.5	0.167	0.40	0.0749	0.0212	0.0962	0.2209
20000.0	1000.00	7.5	0.167	0.10	0.0730	0.0068	0.0798	0.0851
20000.0	1000.00	7.5	0.167	0.20	0.0730	0.0136	0.0866	0.1570
20000.0	1000.00	7.5	0.167	0.30	0.0730	0.0204	0.0934	0.2183
20000.0	1000.00	7.5	0.167	0.40	0.0730	0.0272	0.1002	0.2713
24000.0	1000.00	7.5	0.167	0.10	0.0721	0.0085	0.0807	0.1058
24000.0	1000.00	7.5	0.167	0.20	0.0721	0.0171	0.0892	0.1914
24000.0	1000.00	7.5	0.167	0.30	0.0721	0.0256	0.0977	0.2620
24000.0	1000.00	7.5	0.167	0.40	0.0721	0.0341	0.1063	0.3213

Table 5. Continued

UINF FPS	PINF TORR	THETAL DEG.	RN/RB	RAIL/CIR	CDAERO	CDSI	CDT	CDSI/CDT
12000.0	10.00	10.0	0.0	0.10	0.0989	0.0081	0.1070	0.0755
12000.0	10.00	10.0	0.0	0.20	0.0989	0.0162	0.1151	0.1404
12000.0	10.00	10.0	0.0	0.30	0.0989	0.0242	0.1232	0.1968
12000.0	10.00	10.0	0.0	0.40	0.0989	0.0323	0.1313	0.2462
16000.0	10.00	10.0	0.0	0.10	0.0965	0.0111	0.1076	0.1035
16000.0	10.00	10.0	0.0	0.20	0.0965	0.0223	0.1188	0.1876
16000.0	10.00	10.0	0.0	0.30	0.0965	0.0334	0.1299	0.2572
16000.0	10.00	10.0	0.0	0.40	0.0965	0.0446	0.1411	0.3159
20000.0	10.00	10.0	0.0	0.10	0.0962	0.0148	0.1110	0.1332
20000.0	10.00	10.0	0.0	0.20	0.0962	0.0296	0.1258	0.2352
20000.0	10.00	10.0	0.0	0.30	0.0962	0.0444	0.1406	0.3157
20000.0	10.00	10.0	0.0	0.40	0.0962	0.0592	0.1554	0.3809
24000.0	10.00	10.0	0.0	0.10	0.0967	0.0189	0.1156	0.1636
24000.0	10.00	10.0	0.0	0.20	0.0967	0.0379	0.1346	0.2814
24000.0	10.00	10.0	0.0	0.30	0.0967	0.0568	0.1535	0.3700
24000.0	10.00	10.0	0.0	0.40	0.0967	0.0757	0.1724	0.4392
12000.0	100.00	10.0	0.0	0.10	0.0864	0.0081	0.0945	0.0855
12000.0	100.00	10.0	0.0	0.20	0.0864	0.0162	0.1026	0.1575
12000.0	100.00	10.0	0.0	0.30	0.0864	0.0242	0.1107	0.2190
12000.0	100.00	10.0	0.0	0.40	0.0864	0.0323	0.1188	0.2722
16000.0	100.00	10.0	0.0	0.10	0.0830	0.0111	0.0942	0.1182
16000.0	100.00	10.0	0.0	0.20	0.0830	0.0223	0.1053	0.2116
16000.0	100.00	10.0	0.0	0.30	0.0830	0.0334	0.1164	0.2870
16000.0	100.00	10.0	0.0	0.40	0.0830	0.0446	0.1276	0.3493
20000.0	100.00	10.0	0.0	0.10	0.0820	0.0148	0.0968	0.1528
20000.0	100.00	10.0	0.0	0.20	0.0820	0.0296	0.1116	0.2652
20000.0	100.00	10.0	0.0	0.30	0.0820	0.0444	0.1264	0.3511
20000.0	100.00	10.0	0.0	0.40	0.0820	0.0592	0.1412	0.4192
24000.0	100.00	10.0	0.0	0.10	0.0819	0.0189	0.1008	0.1877
24000.0	100.00	10.0	0.0	0.20	0.0819	0.0379	0.1197	0.3162
24000.0	100.00	10.0	0.0	0.30	0.0819	0.0568	0.1386	0.4095
24000.0	100.00	10.0	0.0	0.40	0.0819	0.0757	0.1576	0.4805
12000.0	1000.00	10.0	0.0	0.10	0.0785	0.0081	0.0866	0.0932
12000.0	1000.00	10.0	0.0	0.20	0.0785	0.0162	0.0947	0.1707
12000.0	1000.00	10.0	0.0	0.30	0.0785	0.0242	0.1028	0.2358
12000.0	1000.00	10.0	0.0	0.40	0.0785	0.0323	0.1109	0.2916
16000.0	1000.00	10.0	0.0	0.10	0.0745	0.0111	0.0857	0.1300
16000.0	1000.00	10.0	0.0	0.20	0.0745	0.0223	0.0968	0.2301
16000.0	1000.00	10.0	0.0	0.30	0.0745	0.0334	0.1080	0.3095
16000.0	1000.00	10.0	0.0	0.40	0.0745	0.0446	0.1191	0.3742
20000.0	1000.00	10.0	0.0	0.10	0.0730	0.0148	0.0878	0.1683
20000.0	1000.00	10.0	0.0	0.20	0.0730	0.0296	0.1026	0.2883
20000.0	1000.00	10.0	0.0	0.30	0.0730	0.0444	0.1174	0.3779
20000.0	1000.00	10.0	0.0	0.40	0.0730	0.0592	0.1322	0.4476
24000.0	1000.00	10.0	0.0	0.10	0.0725	0.0189	0.0914	0.2069
24000.0	1000.00	10.0	0.0	0.20	0.0725	0.0379	0.1104	0.3431
24000.0	1000.00	10.0	0.0	0.30	0.0725	0.0568	0.1293	0.4392
24000.0	1000.00	10.0	0.0	0.40	0.0725	0.0757	0.1482	0.5109

Table 5. Continued

UINF FPS	PINF TORR	THETAC DEG.	RN/RB	RAIL/CIR	CDAERO	CDSI	CDT	CDSI/CDT
12000.0	10.00	10.0	0.100	0.10	0.1075	0.0072	0.1147	0.0627
12000.0	10.00	10.0	0.100	0.20	0.1075	0.0144	0.1219	0.1180
12000.0	10.00	10.0	0.100	0.30	0.1075	0.0216	0.1291	0.1671
12000.0	10.00	10.0	0.100	0.40	0.1075	0.0288	0.1363	0.2111
16000.0	10.00	10.0	0.100	0.10	0.1050	0.0101	0.1151	0.0877
16000.0	10.00	10.0	0.100	0.20	0.1050	0.0202	0.1253	0.1614
16000.0	10.00	10.0	0.100	0.30	0.1050	0.0303	0.1354	0.2240
16000.0	10.00	10.0	0.100	0.40	0.1050	0.0404	0.1455	0.2780
20000.0	10.00	10.0	0.100	0.10	0.1047	0.0136	0.1183	0.1146
20000.0	10.00	10.0	0.100	0.20	0.1047	0.0271	0.1319	0.2057
20000.0	10.00	10.0	0.100	0.30	0.1047	0.0407	0.1454	0.2798
20000.0	10.00	10.0	0.100	0.40	0.1047	0.0543	0.1590	0.3413
24000.0	10.00	10.0	0.100	0.10	0.1052	0.0174	0.1227	0.1422
24000.0	10.00	10.0	0.100	0.20	0.1052	0.0349	0.1401	0.2491
24000.0	10.00	10.0	0.100	0.40	0.1052	0.0698	0.1751	0.3989
24000.0	10.00	10.0	0.100	0.30	0.1052	0.0524	0.1576	0.3323
12000.0	100.00	10.0	0.100	0.10	0.0950	0.0072	0.1022	0.0704
12000.0	100.00	10.0	0.100	0.20	0.0950	0.0144	0.1094	0.1315
12000.0	100.00	10.0	0.100	0.30	0.0950	0.0216	0.1166	0.1851
12000.0	100.00	10.0	0.100	0.40	0.0950	0.0288	0.1238	0.2325
16000.0	100.00	10.0	0.100	0.10	0.0916	0.0101	0.1017	0.0994
16000.0	100.00	10.0	0.100	0.20	0.0916	0.0202	0.1118	0.1809
16000.0	100.00	10.0	0.100	0.30	0.0916	0.0303	0.1219	0.2488
20000.0	100.00	10.0	0.100	0.10	0.0905	0.0136	0.1041	0.1302
20000.0	100.00	10.0	0.100	0.20	0.0905	0.0271	0.1177	0.2306
20000.0	100.00	10.0	0.100	0.30	0.0905	0.0407	0.1312	0.3100
20000.0	100.00	10.0	0.100	0.40	0.0905	0.0543	0.1448	0.3747
24000.0	100.00	10.0	0.100	0.10	0.0904	0.0174	0.1078	0.1618
24000.0	100.00	10.0	0.100	0.20	0.0904	0.0349	0.1253	0.2786
24000.0	100.00	10.0	0.100	0.30	0.0904	0.0524	0.1428	0.3668
24000.0	100.00	10.0	0.100	0.40	0.0904	0.0698	0.1602	0.4358
12000.0	1000.00	10.0	0.100	0.10	0.0871	0.0072	0.0943	0.0762
12000.0	1000.00	10.0	0.100	0.20	0.0871	0.0144	0.1015	0.1418
12000.0	1000.00	10.0	0.100	0.30	0.0871	0.0216	0.1087	0.1985
12000.0	1000.00	10.0	0.100	0.40	0.0871	0.0288	0.1159	0.2483
16000.0	1000.00	10.0	0.100	0.10	0.0831	0.0101	0.0932	0.1084
16000.0	1000.00	10.0	0.100	0.20	0.0831	0.0202	0.1033	0.1957
16000.0	1000.00	10.0	0.100	0.30	0.0831	0.0303	0.1134	0.2674
16000.0	1000.00	10.0	0.100	0.40	0.0831	0.0404	0.1235	0.3274
20000.0	1000.00	10.0	0.100	0.10	0.0816	0.0136	0.0951	0.1425
20000.0	1000.00	10.0	0.100	0.20	0.0816	0.0271	0.1087	0.2495
20000.0	1000.00	10.0	0.100	0.30	0.0816	0.0407	0.1223	0.3327
20000.0	1000.00	10.0	0.100	0.40	0.0816	0.0543	0.1358	0.3994
24000.0	1000.00	10.0	0.100	0.10	0.0810	0.0174	0.0985	0.1772
24000.0	1000.00	10.0	0.100	0.20	0.0810	0.0349	0.1160	0.3011
24000.0	1000.00	10.0	0.100	0.30	0.0810	0.0524	0.1334	0.3925
24000.0	1000.00	10.0	0.100	0.40	0.0810	0.0698	0.1509	0.4629

Table 5. Continued

UINF FPS	PINF 1UXR	THETAC DEG	RN/RB	PAIL/CIR	CDAERO	CDSI	CDT	CDSI/CDT
12000.0	10.00	10.0	0.167	0.10	0.1231	0.0061	0.1291	0.0470
12000.0	10.00	10.0	0.167	0.20	0.1231	0.0121	0.1352	0.0898
12000.0	10.00	10.0	0.167	0.30	0.1231	0.0182	0.1413	0.1289
12000.0	10.00	10.0	0.167	0.40	0.1231	0.0243	0.1473	0.1648
16000.0	10.00	10.0	0.167	0.10	0.1205	0.0085	0.1291	0.0659
16000.0	10.00	10.0	0.167	0.20	0.1205	0.0170	0.1376	0.1237
16000.0	10.00	10.0	0.167	0.30	0.1205	0.0255	0.1461	0.1747
16000.0	10.00	10.0	0.167	0.40	0.1205	0.0340	0.1546	0.2202
20000.0	10.00	10.0	0.167	0.10	0.1202	0.0114	0.1316	0.0865
20000.0	10.00	10.0	0.167	0.20	0.1202	0.0228	0.1430	0.1594
20000.0	10.00	10.0	0.167	0.30	0.1202	0.0342	0.1544	0.2214
20000.0	10.00	10.0	0.167	0.40	0.1202	0.0456	0.1658	0.2750
24000.0	10.00	10.0	0.167	0.10	0.1207	0.0147	0.1354	0.1082
24000.0	10.00	10.0	0.167	0.20	0.1207	0.0293	0.1500	0.1954
24000.0	10.00	10.0	0.167	0.30	0.1207	0.0440	0.1647	0.2670
24000.0	10.00	10.0	0.167	0.40	0.1207	0.0586	0.1794	0.3269
12000.0	100.00	10.0	0.167	0.10	0.1105	0.0061	0.1166	0.0520
12000.0	100.00	10.0	0.167	0.20	0.1105	0.0121	0.1227	0.0990
12000.0	100.00	10.0	0.167	0.30	0.1105	0.0182	0.1288	0.1414
12000.0	100.00	10.0	0.167	0.40	0.1105	0.0243	0.1348	0.1801
16000.0	100.00	10.0	0.167	0.10	0.1071	0.0085	0.1156	0.0736
16000.0	100.00	10.0	0.167	0.20	0.1071	0.0170	0.1241	0.1371
16000.0	100.00	10.0	0.167	0.30	0.1071	0.0255	0.1326	0.1924
16000.0	100.00	10.0	0.167	0.40	0.1071	0.0340	0.1411	0.2411
20000.0	100.00	10.0	0.167	0.10	0.1060	0.0114	0.1174	0.0970
20000.0	100.00	10.0	0.167	0.20	0.1060	0.0228	0.1288	0.1770
20000.0	100.00	10.0	0.167	0.30	0.1060	0.0342	0.1402	0.2438
20000.0	100.00	10.0	0.167	0.40	0.1060	0.0456	0.1516	0.3007
24000.0	100.00	10.0	0.167	0.10	0.1059	0.0147	0.1205	0.1215
24000.0	100.00	10.0	0.167	0.20	0.1059	0.0293	0.1352	0.2169
24000.0	100.00	10.0	0.167	0.30	0.1059	0.0440	0.1499	0.2934
24000.0	100.00	10.0	0.167	0.40	0.1059	0.0586	0.1645	0.3564
12000.0	1000.00	10.0	0.167	0.10	0.1026	0.0061	0.1087	0.0558
12000.0	1000.00	10.0	0.167	0.20	0.1026	0.0121	0.1148	0.1058
12000.0	1000.00	10.0	0.167	0.30	0.1026	0.0182	0.1209	0.1507
12000.0	1000.00	10.0	0.167	0.40	0.1026	0.0243	0.1269	0.1913
16000.0	1000.00	10.0	0.167	0.10	0.0986	0.0085	0.1071	0.0794
16000.0	1000.00	10.0	0.167	0.20	0.0986	0.0170	0.1156	0.1472
16000.0	1000.00	10.0	0.167	0.30	0.0986	0.0255	0.1241	0.2056
16000.0	1000.00	10.0	0.167	0.40	0.0986	0.0340	0.1326	0.2566
20000.0	1000.00	10.0	0.167	0.10	0.0971	0.0114	0.1085	0.1050
20000.0	1000.00	10.0	0.167	0.20	0.0971	0.0228	0.1199	0.1902
20000.0	1000.00	10.0	0.167	0.30	0.0971	0.0342	0.1313	0.2604
20000.0	1000.00	10.0	0.167	0.40	0.0971	0.0456	0.1427	0.3196
24000.0	1000.00	10.0	0.167	0.10	0.0965	0.0147	0.1112	0.1318
24000.0	1000.00	10.0	0.167	0.20	0.0965	0.0293	0.1259	0.2330
24000.0	1000.00	10.0	0.167	0.30	0.0965	0.0440	0.1405	0.3130
24000.0	1000.00	10.0	0.167	0.40	0.0965	0.0586	0.1552	0.3779

Table 5. Continued

UINF FPS	FINF TORR	THETAC DEG.	RN/RB	RAIL/CIR	CDAERO	CDSI	CDT	CDSI/CDT
12000.0	10.00	10.0	0.200	0.10	0.1337	0.0060	0.1397	0.0429
12000.0	10.00	10.0	0.200	0.20	0.1337	0.0120	0.1457	0.0824
12000.0	10.00	10.0	0.200	0.30	0.1337	0.0180	0.1517	0.1186
12000.0	10.00	10.0	0.200	0.40	0.1337	0.0240	0.1577	0.1522
16000.0	10.00	10.0	0.200	0.10	0.1312	0.0084	0.1396	0.0598
16000.0	10.00	10.0	0.200	0.20	0.1312	0.0167	0.1479	0.1130
16000.0	10.00	10.0	0.200	0.30	0.1312	0.0251	0.1563	0.1604
16000.0	10.00	10.0	0.200	0.40	0.1312	0.0334	0.1646	0.2030
20000.0	10.00	10.0	0.200	0.10	0.1309	0.0111	0.1420	0.0785
20000.0	10.00	10.0	0.200	0.20	0.1309	0.0223	0.1532	0.1457
20000.0	10.00	10.0	0.200	0.30	0.1309	0.0335	0.1643	0.2036
20000.0	10.00	10.0	0.200	0.40	0.1309	0.0446	0.1755	0.2543
24000.0	10.00	10.0	0.200	0.10	0.1313	0.0143	0.1457	0.0982
24000.0	10.00	10.0	0.200	0.20	0.1313	0.0286	0.1600	0.1790
24000.0	10.00	10.0	0.200	0.30	0.1313	0.0429	0.1743	0.2464
24000.0	10.00	10.0	0.200	0.40	0.1313	0.0573	0.1886	0.3037
12000.0	100.00	10.0	0.200	0.10	0.1212	0.0060	0.1272	0.0472
12000.0	100.00	10.0	0.200	0.20	0.1212	0.0120	0.1332	0.0901
12000.0	100.00	10.0	0.200	0.30	0.1212	0.0180	0.1392	0.1293
12000.0	100.00	10.0	0.200	0.40	0.1212	0.0240	0.1452	0.1653
16000.0	100.00	10.0	0.200	0.10	0.1177	0.0084	0.1261	0.0662
16000.0	100.00	10.0	0.200	0.20	0.1177	0.0167	0.1345	0.1243
16000.0	100.00	10.0	0.200	0.40	0.1177	0.0334	0.1512	0.2211
16000.0	100.00	10.0	0.200	0.30	0.1177	0.0251	0.1428	0.1755
20000.0	100.00	10.0	0.200	0.10	0.1167	0.0111	0.1278	0.0872
20000.0	100.00	10.0	0.200	0.20	0.1167	0.0223	0.1390	0.1605
20000.0	100.00	10.0	0.200	0.30	0.1167	0.0335	0.1501	0.2229
20000.0	100.00	10.0	0.200	0.40	0.1167	0.0446	0.1613	0.2767
24000.0	100.00	10.0	0.200	0.10	0.1165	0.0143	0.1308	0.1094
24000.0	100.00	10.0	0.200	0.20	0.1165	0.0286	0.1452	0.1973
24000.0	100.00	10.0	0.200	0.30	0.1165	0.0429	0.1595	0.2693
24000.0	100.00	10.0	0.200	0.40	0.1165	0.0573	0.1738	0.3296
12000.0	1000.00	10.0	0.200	0.10	0.1133	0.0060	0.1193	0.0503
12000.0	1000.00	10.0	0.200	0.20	0.1133	0.0120	0.1253	0.0958
12000.0	1000.00	10.0	0.200	0.30	0.1133	0.0180	0.1313	0.1371
12000.0	1000.00	10.0	0.200	0.40	0.1133	0.0240	0.1373	0.1748
16000.0	1000.00	10.0	0.200	0.10	0.1093	0.0084	0.1176	0.0710
16000.0	1000.00	10.0	0.200	0.20	0.1093	0.0167	0.1260	0.1327
16000.0	1000.00	10.0	0.200	0.30	0.1093	0.0251	0.1343	0.1866
16000.0	1000.00	10.0	0.200	0.40	0.1093	0.0334	0.1427	0.2343
20000.0	1000.00	10.0	0.200	0.10	0.1077	0.0111	0.1189	0.0938
20000.0	1000.00	10.0	0.200	0.20	0.1077	0.0223	0.1300	0.1716
20000.0	1000.00	10.0	0.200	0.30	0.1077	0.0335	0.1412	0.2370
20000.0	1000.00	10.0	0.200	0.40	0.1077	0.0446	0.1523	0.2929
24000.0	1000.00	10.0	0.200	0.10	0.1072	0.0143	0.1215	0.1178
24000.0	1000.00	10.0	0.200	0.20	0.1072	0.0286	0.1358	0.2109
24000.0	1000.00	10.0	0.200	0.30	0.1072	0.0429	0.1501	0.2861

Table 5. Concluded

UI F PRS	PINF TURB	INITIAL DELTA	RN/RB	FAIL/GIR	CDAERO	CDSI	CDT	CDSI/CDT
12000.0	10.00	10.0	0.300	0.10	0.1772	0.0065	0.1837	0.0352
12000.0	10.00	10.0	0.300	0.20	0.1772	0.0130	0.1902	0.0681
12000.0	10.00	10.0	0.300	0.30	0.1772	0.0194	0.1967	0.0988
12000.0	10.00	10.0	0.300	0.40	0.1772	0.0259	0.2031	0.1275
16000.0	10.00	10.0	0.300	0.10	0.1746	0.0089	0.1835	0.0484
16000.0	10.00	10.0	0.300	0.20	0.1746	0.0178	0.1924	0.0924
16000.0	10.00	10.0	0.300	0.30	0.1746	0.0267	0.2013	0.1324
16000.0	10.00	10.0	0.300	0.40	0.1746	0.0356	0.2102	0.1691
20000.0	10.00	10.0	0.300	0.10	0.1743	0.0116	0.1860	0.0633
20000.0	10.00	10.0	0.300	0.20	0.1743	0.0236	0.1978	0.1191
20000.0	10.00	10.0	0.300	0.30	0.1743	0.0353	0.2046	0.1686
20000.0	10.00	10.0	0.300	0.40	0.1743	0.0471	0.2214	0.2128
24000.0	10.00	10.0	0.300	0.10	0.1747	0.0150	0.1898	0.0793
24000.0	10.00	10.0	0.300	0.20	0.1747	0.0301	0.2049	0.1470
24000.0	10.00	10.0	0.300	0.30	0.1747	0.0452	0.2199	0.2053
24000.0	10.00	10.0	0.300	0.40	0.1747	0.0602	0.2350	0.2563
12000.0	100.00	10.0	0.300	0.10	0.1647	0.0065	0.1712	0.0378
12000.0	100.00	10.0	0.300	0.20	0.1647	0.0130	0.1777	0.0729
12000.0	100.00	10.0	0.300	0.30	0.1647	0.0194	0.1841	0.1055
12000.0	100.00	10.0	0.300	0.40	0.1647	0.0259	0.1906	0.1359
16000.0	100.00	10.0	0.300	0.10	0.1612	0.0089	0.1701	0.0522
16000.0	100.00	10.0	0.300	0.20	0.1612	0.0178	0.1790	0.0993
16000.0	100.00	10.0	0.300	0.30	0.1612	0.0267	0.1878	0.1419
16000.0	100.00	10.0	0.300	0.40	0.1612	0.0356	0.1967	0.1807
20000.0	100.00	10.0	0.300	0.10	0.1601	0.0118	0.1719	0.0685
20000.0	100.00	10.0	0.300	0.20	0.1601	0.0236	0.1836	0.1283
20000.0	100.00	10.0	0.300	0.30	0.1601	0.0353	0.1954	0.1808
20000.0	100.00	10.0	0.300	0.40	0.1601	0.0471	0.2072	0.2274
24000.0	100.00	10.0	0.300	0.10	0.1599	0.0150	0.1750	0.0860
24000.0	100.00	10.0	0.300	0.20	0.1599	0.0301	0.1900	0.1585
24000.0	100.00	10.0	0.300	0.30	0.1599	0.0452	0.2051	0.2202
24000.0	100.00	10.0	0.300	0.40	0.1599	0.0602	0.2201	0.2736
12000.0	1000.00	10.0	0.300	0.10	0.1568	0.0065	0.1633	0.0396
12000.0	1000.00	10.0	0.300	0.20	0.1568	0.0130	0.1698	0.0763
12000.0	1000.00	10.0	0.300	0.30	0.1568	0.0194	0.1762	0.1102
12000.0	1000.00	10.0	0.300	0.40	0.1568	0.0259	0.1827	0.1418
16000.0	1000.00	10.0	0.300	0.10	0.1527	0.0089	0.1616	0.0550
16000.0	1000.00	10.0	0.300	0.20	0.1527	0.0178	0.1705	0.1043
16000.0	1000.00	10.0	0.300	0.30	0.1527	0.0267	0.1794	0.1486
16000.0	1000.00	10.0	0.300	0.40	0.1527	0.0356	0.1883	0.1889
20000.0	1000.00	10.0	0.300	0.10	0.1511	0.0118	0.1629	0.0723
20000.0	1000.00	10.0	0.300	0.20	0.1511	0.0236	0.1747	0.1349
20000.0	1000.00	10.0	0.300	0.30	0.1511	0.0353	0.1865	0.1895
20000.0	1000.00	10.0	0.300	0.40	0.1511	0.0471	0.1982	0.2377
24000.0	1000.00	10.0	0.300	0.10	0.1506	0.0150	0.1656	0.0909
24000.0	1000.00	10.0	0.300	0.20	0.1506	0.0301	0.1807	0.1667
24000.0	1000.00	10.0	0.300	0.30	0.1506	0.0452	0.1957	0.2307
24000.0	1000.00	10.0	0.300	0.40	0.1506	0.0602	0.2108	0.2857

These solutions will allow the interested reader to make graphical studies not included in the present report.

The present experimental and analytic investigations indicate the approximate magnitude of aerodynamic drag which will be induced because of the bow shock interaction between the track and a model traveling down a constraining track system. Although it is clear that additional experimental data are required to confirm or improve the analysis, the following parameters (in decreasing order) have been shown to be important:

1. Model Cone Angle and Bluntness

    The relative importance of shock interaction drag in terms of total drag increases with increasing cone angle and decreasing bluntness ratio (Figs. 22, 23, and 25) except for small V_∞ and θ_c.

2. Model Velocity

    The term $C_{D_{SI}}/C_{D_T}$ increases very rapidly with increasing velocity (Fig. 20). In terms of practical ballistic coefficient, an optimum velocity results for a given model and track configuration (Fig. 21). A combination of high cone angle and model velocity results in greater than 40 percent of the total deceleration force being caused by model bow shock interaction (Fig. 25).

3. Rail Width

    The contribution of shock interference drag is reduced as rail width decreases (Fig. 26).

4. Range Pressure

    Shock interference drag is sensitive to range pressures at levels below about 100 torr but is not a strong influence above this level (Figs. 20 and 21).

5. Track Sliding Friction

    Although this term was studied only qualitatively, it was shown to have a potentially large influence if the absolute value is greater than about 100 lbf (Figs. 27 and 28).

REFERENCES

1. Teng, Robert N., Hickman, Roy. S, and Sutila, George E. "Development of a Scaled-Up Hypervelocity Projectile Guiding and Retrieving System." AEDC-TR-74-123 (ADB001028L), January 1975.

2. Pate, S. R. and Eaves, R. H., Jr. "Recent Advances in the Performance and Testing Capabilities of the AEDC-VKF Tunnel F (HOTSHOT) Hypersonic Facility." AIAA Paper No. 74-84, presented at the AIAA 12th Aerospace Sciences Meeting, Washington, D.C., January 30 - February 1, 1974.

3. Ledford, R. L., Smotherman, W. E., and Kidd, C. T. "Recent Developments in Heat-Transfer-Rate, Pressure, and Force Measurements for HOTSHOT Tunnels." AEDC-TR-66-228 (AD645764), January 1967.

4. Bynum, D. S. "Instrumentation for the AEDC/VKF 100-in. Hotshot (Tunnel F)." AEDC-TR-66-209 (AD804567), January 1967.

5. Fay, J. A. and Riddell, F. R. "Theory of Stagnation Point Heat Transfer in Dissociated Air." Journal of the Aeronautical Sciences, Vol. 25, No. 2. February 1958, pp. 73-85, 121.

6. Brahinsky, Herbert S. and Neel, Charles A. "Tables of Equilibrium Thermodynamic Properties of Nitrogen, Vols. I-IV." AEDC-TR-69-126 (AD693134, AD692712, AD692713, and AD692172), August 1969.

7. Grabau, Martin, Smithson, H. K., Jr., and Little, W. J. "A Data Reduction Program for Hotshot Tunnels Based on the Fay-Riddell Heat-Transfer Rate Using Nitrogen at Stagnation Temperatures from 1500 to 5000°K." AEDC-TDR-64-50 (AD601070), June 1964.

8. Griffith, B. J. and Lewis, Clark H. "Laminar Heat Transfer to Spherically Blunted Cones at Hypersonic Conditions." AIAA Journal, Vol. 2, No. 3, March 1964, pp. 438-444.

9. Boudreau, A. H. "Aerodynamic Force Measurements on a Star-Cross-Section Reentry Vehicle." AEDC-TR-74-95 (AD922970L), September 1974.

10. Clark, E. L. and Trimmer, L. L. "Equations and Charts for the Evaluation of the Hypersonic Aerodynamic Characteristics of Lifting Configurations by the Newtonian Theory." AEDC-TDR-64-25 (AD431848), March 1964.

11. Jones, D. J. "Tables of Inviscid Supersonic Flow About Circular Cones at Incidence $\gamma = 1.4$." AGARDograph 137, November 1969.

12. Shapiro, Ascher H. The Dynamics and Thermodynamics of Compressible Fluid Flow (Vol. 1, pp. 451-452). The Ronald Press Company, New York, 1953.

13. Trimmer, L. L. "Equations and Charts for the Evaluation of Forces on Spherically Blunted Cones by the Newtonian Theory." AEDC-TR-66-16 (AD631149), April 1966.

14. Katsikas, C. J., Castle, G. K. and Higgins, J. S. "Ablation Handbook—Entry Materials Data and Design." AFML-TR-66-262, November 1966.

NOMENCLATURE

A	Reference area, πr_b^2
B	Ballistic coefficient [Eq. (19)]
C_{A_i}	Inviscid axial-force coefficient
C_{A_t}	Total measured axial-force coefficient
C_{D_B}	Aerodynamic base drag coefficient [Eqs. (1) and (18)]
$C_{D_{BL}}$	Baseline drag coefficient measured with no track system in place
C_{D_F}	Drag coefficient attributable to sliding friction between model cylinder and rail [Eqs. (1) and (14)]
$C_{D_{IP}}$	Aerodynamic viscous-induced pressure drag coefficient [Eq. (1)]
C_{D_P}	Aerodynamic pressure drag coefficient [Eqs. (1) and (15)]
$C_{D_{SI}}$	Drag coefficient attributable to shock interaction forces between model and rail [Eqs. (1) and (3)]
C_{D_T}	Total drag coefficient of a ballistic range model traveling in a constraining track system [Eq. (1)]
C_{D_V}	Aerodynamic viscous drag coefficient [Eqs. (1) and (16)]
$C_{P_{max}}$	Maximum pressure coefficient
D_{SI}	Shock interaction drag [Eq. (2)]
F	Mass fraction term in Eq. (16)
FD	Sliding friction drag
H^*	Reference enthalpy defined by Eq. (17)
He	Gas enthalpy at edge of boundary layer
Ho	Stagnation enthalpy
K	An empirical correction factor defined by Eqs. (2) and (7)

L	Position of rail leading edge in relation to cone-cylinder junction (Fig. 1)
ℓ, ℓ_1, ℓ_2	Characteristic lengths of model (Fig. 5)
ℓ_s	Sharp cone length
M_e	Mach number at edge of boundary layer
M_s	Local Mach number after first reflection (Fig. 9)
M_∞	Free-stream Mach number
p_b	Base pressure
p_e	Local pressure at edge of boundary layer
p_o	Stagnation chamber pressure
p_o'	Pitot pressure
p_s	Local pressure after first shock reflection (Fig. 9)
p_w	Wall pressure
p_∞	Free-stream static pressure
$\dot{q}_o$	Stagnation point Fay-Riddell heat-transfer rate
q_∞	Free-stream dynamic pressure
R	Gas constant
Re	Unit free-stream Reynolds number per foot
Re_ℓ	Free-stream Reynolds number based on characteristic length ℓ
Re_{ℓ_s}	Free-stream Reynolds number based on sharp cone length, ℓ_s
RW	Rail width
r_b	Model base radius, assumed to be equal to track inside radius
r_n	Model nose radius
T_e	Temperature at edge of boundary layer

T_o	Stagnation temperature
T_w	Wall temperature
T_∞	Free-stream static temperature
TD	Track diameter
V_e	Velocity at edge of boundary layer
V_∞	Free-stream velocity
W	Model weight
x	Cone distance influenced by shock reflection (Fig. 9)
x_1	Axial distance measured from nose
x_b	Cone distance influenced by blunt body shock reflection (Fig. 10)
x_s	Cone distance influenced by sharp body shock reflection (Fig. 10)
Y	Correction to the parameter K for cone angles other than 10 deg [Eq. (9)]
y	Distance from cone centerline
Z	Correction to the parameter K for bluntness ratios other than 0.167 [Eqs. (10) through (13)]
a	Angle of attack
γ	Ratio of specific heats
θ_c	Cone half-angle (Fig. 9)
θ_s	Local model bow shock angle (Fig. 9)
θ_s'	Model bow shock angle after first reflection from rail (Fig. 9)
ξ	Nose bluntness ratio, r_n/r_b
ρ_∞	Free-stream density